The Precipitation Rate Retrieval Algorithms
for the GPM Dual-frequency Precipitation Radar

Shinta SETO

Graduate School of Engineering, Nagasaki University, Nagasaki, Japan

Toshio IGUCHI

University of Maryland, ESSIC, Maryland, USA

Robert MENEGHINI

NASA Goddard Space Flight Center, Maryland, USA

Jun AWAKA

Tokai University (Emeritus Professor), Sapporo, Japan

Takuji KUBOTA

Earth Observation Research Center, Japan Aerospace Exploration Agency, Tsukuba, Japan

Takeshi MASAKI

Remote Sensing Technology Center of Japan, Tsukuba, Japan

and

Nobuhiro TAKAHASHI

Institute for Space-Earth Environmental Research, Nagoya University, Nagoya, Japan

(Manuscript received 13 May 2020, in final form 30 October 2020)

Abstract

In this paper, precipitation rate retrieval algorithms for the Global Precipitation Measurement mission's Dual-frequency Precipitation Radar (DPR) are developed. The DPR consists of a Ku-band radar (KuPR; 13.6 GHz) and a Ka-band radar (KaPR; 35.5 GHz). For the KuPR, an algorithm similar to the Tropical Rainfall Measuring Mission's Precipitation Radar algorithm is developed, with the relation between precipitation rate R and mass-weighted mean diameter D_m ($R-D_m$ relation) replacing the relation between the specific attenuation k and effective radar reflectivity factor Z_e. The $R-D_m$ relation can also be applied to the KaPR and dual-frequency algorithms. In both the single-frequency and dual-frequency algorithms, the forward retrieval method is applied with an as-

Corresponding author: Shinta Seto, Graduate School of Engineering, Nagasaki University, 1-14, Bunkyo-machi, Nagasaki-shi, Nagasaki 852-8521, Japan
E-mail: seto@nagasaki-u.ac.jp

sumed adjustment factor for the $R-D_m$ relation (ε) and the results are evaluated to select the best value of ε. The advantages of the dual-frequency algorithm are the availability of the dual-frequency surface reference technique and the ZfKa method, which is a method to use the attenuation-corrected radar reflectivity factor Z_f of KaPR, to select ε as well as the possibility to selectively use measurements from KuPR or KaPR. This paper also describes the derivation of the scattering table and the $R-D_m$ relation as well as the procedure for non-uniform beam filling correction in detail. The outputs are then statistically analyzed to demonstrate algorithm performance.

1.   Introduction

1.1   Overview of DPR

The Dual-frequency Precipitation Radar (DPR) instrument is carried on the core satellite of the Global Precipitation Measurement (GPM) mission (Kojima et al. 2012; Iguchi 2020; Masaki et al. 2021). The GPM core satellite started operations in March 2014 (Hou et al. 2014; Skofronick-Jackson et al. 2017). The satellite orbits the Earth about 16 times per day in a non-sun-synchronous orbit between 65°S and 65°N. The DPR consists of a Ku-band radar (KuPR; 13.6 GHz) and a Ka-band radar (KaPR; 35.5 GHz), which have a horizontal resolution of approximately 5 km at the surface.

As shown in Fig. 1, the KuPR observes 49 pixels (blue circles) per scan. An angle bin number from 1 to 49 is given successively to each pixel or field of view (FOV), with angle bin 25 associated with nadir viewing. During one scan by the KuPR, the KaPR observes 25 pixels (red circles) that are coincident with the inner swath of the KuPR and 24 pixels (green circles) in an interleaved scan. Angle bin numbers from 1 to 25 are assigned to the pixels of the KaPR's normal scan, which are collocated with KuPR's pixels with angle bin numbers from 13 to 37. Dual-frequency measurements are available in this inner swath of the 25 FOV, and the pixels are known as dual-frequency measurement pixels.

The KuPR and KaPR (normal scan) channels have a range resolution of 250 m, but echo power measurements are made every 125 m, a process known as oversampling. Similarly, the KaPR (interleaved scan) has a 500 m range resolution, but measures echo power every 250 m. As the latter has a coarser range resolution but higher sensitivity, it is known as high-sensitivity mode KaPR (KaHS).

The scan pattern described above was in operation until May 21, 2018, after which the KaPR was modified by redirecting interleaved scan KaHS pixels to the outer swath to make coincident Ku-band and Ka-band data available over the full 49-pixel swath (Iguchi 2020). This scan pattern has remained in effect since then. In this paper, only observations from before the scan pattern change are considered.

The KuPR radar is the successor to the Precipitation Radar (PR) instrument on the Tropical Rainfall Measuring Mission (TRMM) satellite, which operated from 1997 to 2015 (Kummerow et al. 1998; Kozu et al. 2001; Takahashi et al. 2016). KuPR and PR have the same scan patterns and horizontal resolution (after TRMM underwent an orbit altitude change in 2001). PR had a range resolution of 250m where, outside of the central swath, echo power was measured at an interval of 250m (i.e., no oversampling). The difference in frequencies between PR (13.8 GHz) and KuPR (13.6 GHz) is small and is thus neglected in this study.

1.2   DPR algorithms

The DPR standard Level-1 algorithm is independently applied to KuPR and KaPR data and outputs such as echo power, noise power, measurement time, and location are stored in the respective KuPR and KaPR Level-1 data products (Masaki et al. 2021). The DPR standard Level-2 algorithms (hereafter, DPR algorithms) consist of three algorithms: the KuPR, KaPR, and dual-frequency algorithms (Kubota et al. 2014; Iguchi et al. 2018; Iguchi 2020). The KuPR algorithm uses the KuPR Level-1 product as input and is applied to the blue pixels in Fig. 1. The KaPR algorithm uses the KaPR Level-1 product as input and is applied to the red and green pixels in Fig. 1. The KuPR and KaPR algorithms are single-frequency algorithms and output KuPR and KaPR Level-2 data

products, respectively. The dual-frequency algorithm can use measurements from either KuPR or KaPR, or from both when available, and is applied to all pixels (blue, red, and green) shown in Fig. 1. In the inner swath where both Ku-band and Ka-band data are available, three estimates are generated by the KuPR, KaPR, and dual-frequency algorithms. Outside of the coincident pixels in the inner swath, the dual-frequency algorithm basically functions as a single-frequency algorithm. The dual-frequency algorithm's outputs are stored in the dual-frequency Level-2 data product.

1.3 Modules

Each of the DPR algorithms (KuPR, KaPR, and dual-frequency) consists of six modules as shown in Fig. 2. In the single-frequency algorithms, the six modules are executed twice, whereas they are executed only once in the dual-frequency algorithm. The role of each module is briefly explained below. A more detailed description can be found in Iguchi et al. (2018).

a. Preparation module

From the signal level of the radar return power recorded at each range bin, measured radar reflectivity factors are computed for range bins where the signal level exceeds the noise level by a prescribed amount. The surface-level range bin is determined and the surface backscattering cross section is then calculated. Next, contamination of the precipitation return by surface returns from the main antenna lobe or sidelobes is searched for. Clutter-removal techniques developed by Kubota et al. (2016) and Kubota et al. (2018) are then applied to the KuPR and KaPR data, respectively.

b. Vertical profile module

Vertical profiles of atmospheric variables such as air temperature (denoted by T), air pressure, and humidity are derived from environmental grid data based on the Japan Meteorological Agency's Global Analysis dataset. In the second loop of the single-frequency algorithms, a cloud liquid water (CLW) database is used to provide a vertical CLW profile as a function of the surface precipitation rate and precipitation type estimated in the first loop. In the dual-frequency algorithm, the CLW database is used by referring to the surface precipitation rate and precipitation type estimated by the single-frequency algorithms. Next, attenuation due to non-precipitating particles (e.g., CLW) and atmospheric gases (e.g., oxygen and water vapor) is calculated and the radar reflectivity factor is corrected (Kubota et al. 2020). In this paper, Z_m denotes the radar reflectivity factor corrected for

non-precipitating particles and atmospheric gases.

c. Classification module

The variables Z_m and T are used to search for a bright band (BB). If a BB is detected, the top, peak, and bottom range bins of the BB are determined. Classification of the precipitation type, such as stratiform and convective precipitation, is also performed. Details of the precipitation type classification method are described by Awaka et al. (2016, 2020) and Le et al. (2016).

d. Surface reference technique module

In the surface reference technique (SRT), path integrated attenuation (PIA) is estimated as the difference between the apparent surface backscattering cross sections measured outside and inside the area of precipitation. Details of the SRT can be found in Meneghini et al. (2015, 2020) and Meneghini and Kim (2017). The SRT module uses measured surface backscattering cross section output from the Preparation module. This output has not been corrected for non-precipitating particles or atmospheric gases; therefore, the PIA value estimated by the SRT includes the effects of non-precipitating particles and atmospheric gases. The PIA estimates are then corrected for attenuation by non-precipitating particles and atmospheric gases in the Solver module. The corrected value is denoted by PIA_{SRT}.

e. DSD module

A relation between the precipitation rate (denoted by R) and the mass-weighted mean drop size (denoted by D_m) is assumed ($R-D_m$ relation) as a constraint for the DSD. An integer variable "phase" is then assigned to each range bin as an index to refer to the scattering table. For range bins with liquid precipitation, phase $= 200 + T$, where T is air temperature (°C). The phase variable is set to 100, 150, and 200 at the top, peak, and bottom of the BB, respectively. Above the BB or 0°C height, phase $= 100 + T$.

f. Solver module

A precipitation rate retrieval algorithm is applied in the Solver module. From the inputs such as Z_m, PIA_{SRT}, $R-D_m$ relation, and phase, the outputs such as R, the DSD parameters (D_m and N_w), the effective radar reflectivity factor (Z_e), and specific attenuation (k) are estimated. The final estimate of PIA (PIA_{fin}) is then calculated from the profile of k. For the estimation process, a non-uniform beam filling (NUBF) correction is applied in the second loop of

the single-frequency algorithms using estimates in the first loop; however, the NUBF correction is bypassed in the first loop of the single-frequency algorithms because it requires estimates at surrounding pixels. In the dual-frequency algorithm, the NUBF correction is applied by referring to estimates from a single-frequency algorithm.

1.4   Purpose of this study

To develop the precipitation rate retrieval algorithms of the DPR algorithms, the PR standard algorithm 2A25 (PR algorithm for short; Iguchi et al. 2000, 2009) is regarded as a precursor. For the KuPR algorithm, the precipitation rate retrieval algorithm is basically the same as the PR algorithm. The same structure and common physical assumptions are used as much as possible in all three DPR algorithms. The dual-frequency algorithm has some additional options and is thus expected to give better estimates than the single-frequency algorithms.

In the pre-launch phase, Seto et al. (2013) developed a precipitation retrieval algorithm that is applicable to both single-frequency and dual-frequency measurements. The revised precipitation rate retrieval algorithm (Seto and Iguchi 2015) was applied to the DPR algorithms in version 03B, which was released in September 2014. In version 03B, neither the NUBF correction nor the $R-D_m$ relation were used, and the dual-frequency algorithm sometimes gave unstable estimates. After modifications, version 06A was released in October 2018 (Iguchi and Meneghini 2016a, b, 2017). The basic functions of the KuPR algorithm in version 06A are also applied to TRMM PR standard algorithm version 8, which was released in July 2018 (Tropical Rainfall Measuring Mission 2018), to ensure continuity between PR and KuPR precipitation retrievals. This paper describes the precipitation rate retrieval algorithm in version 06A. After the scan pattern change, version 06A ignores the KaHS and returns missing values for interleaved scans, whereas the experimental product (version 06X) uses KaHS in the outer swath. As noted earlier, only observations before the scan pattern change are used in this study; therefore, version 06X shall be explored in a future publication. In the next version, the algorithm will be applied both before and after the scan pattern change.

The remainder of this paper is structured as follows. In Section 2, the precipitation rate retrieval algorithm framework is explained using some simplifying assumptions. In Sections 3 and 4, the scattering table and $R-D_m$ relation are derived, respectively. In Section 5, the NUBF correction method is explained. In
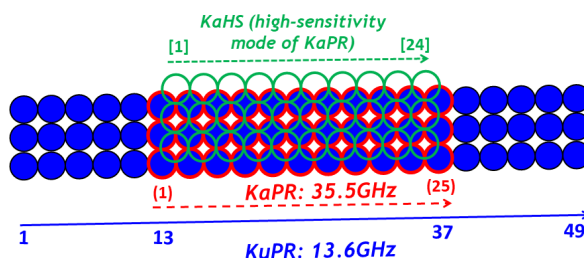

Fig. 1.   A schematic figure of the scan pattern of DPR (before May 21, 2018).

Sections 6 and 7, the single-frequency and the dual-frequency precipitation rate retrieval algorithms are respectively explained in detail without simplifying assumptions. In Section 8, the KuPR, KaPR, and dual-frequency Level-2 products are statistically analyzed to check the performance of the precipitation rate retrieval algorithms and assess the advantages of the dual-frequency algorithm. Lastly, Section 9 provides a summary.

2.   Framework of the precipitation rate retrieval algorithm

In this section, the precipitation rate retrieval algorithm framework is explained using some simplifying assumptions.

2.1   Settings

Z_m is obtained for *n* range bins from the storm top to the surface. The width of the range bin is set to *L* (km), which is 0.125 km for the normal scan and 0.25 km for the interleaved scan. Z_m is assumed to be the average value of *L*, ignoring the effect of oversampling. Range bin numbers are given from top to bottom, with range bin 1 being at the storm top and range bin *n* being at the surface. PIA_{SRT} is assumed to be available.

Let *D* (mm) and *N* (mm^{-1} m^{-3}) be the drop size diameter and number density per diameter, respectively. DSD function $N(D)$ is assumed to follow a Gamma distribution as

$$N(D) = N_w f(D; D_m),   \tag{1}$$

where

$$f(D; D_m) = \frac{6(\mu+4)^{\mu+4}}{4^4 \Gamma(\mu+4)} \left(\frac{D}{D_m}\right)^{\mu} \exp\left[\frac{-(\mu+4)D}{D_m}\right],   \tag{2}$$

where Γ is the Gamma function with the value of μ fixed at 3. N_w (mm^{-1} m^{-3}) and D_m (mm) are the DSD parameters to be retrieved. D_m is the mass-weighted
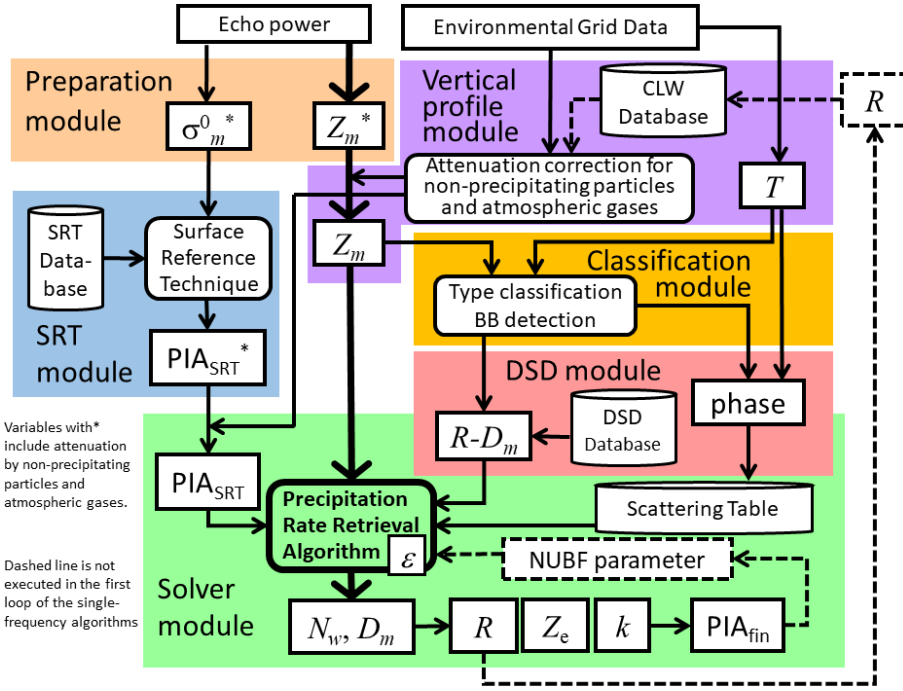
Fig. 2.   A flow chart of DPR algorithms.

mean diameter. which is defined as

$$D_m = \frac{\int_{D=0}^{\infty} D^4 N(D) dD}{\int_{D=0}^{\infty} D^3 N(D) dD}. \tag{3}$$

2.2   Equations

Z_e (mm^6 m^{-3}), k (dB km^{-1}), and R (mm h^{-1}) are functions of the DSD parameters as

$$Z_e = N_w f_z(D_m), \tag{4}$$

$$k = N_w f_k(D_m), \tag{5}$$

and $R = N_w f_R(D_m)c(h), \tag{6}$

where f_Z, f_k, and f_R are derived in Section 3, h is the height (km) from the ellipsoid, and $c(h)$ is a correction factor. Because of low air density in the upper atmosphere, the precipitation particles have a higher fall speed, thus R can be empirically corrected using the term $c(h)$, which is a function of height. $c(h)$ is shown in Fig. 3. At $h = 0$, $c(h) = 1$.

At the distance l ($0 \leq l \leq L$) below the top of range bin i, the measured radar reflectivity factor is theoretically expressed as
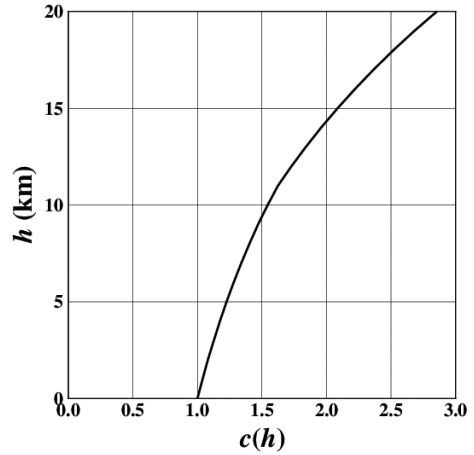

Fig. 3.   Correction factors for precipitation rate at different heights.

$$Z_m(l) = Z_{e,i} 10^{-0.2K_i L - 0.2k_i l}, \tag{7}$$

where $K_i \equiv \sum_{j=1}^{i-1} k_j, \tag{8}$

where j is a dummy variable for the range bin number. $Z_{e,i}$ and k_i are the effective radar reflectivity factor and

specific attenuation at range bin i, respectively. These values are assumed to be constant for $0 \leq l \leq L$.

By taking the average of $Z_m(l)$ from $l = 0$ to $l = L$, Z_m at range bin i can be calculated as

$$
\begin{aligned}
Z_{m,i} &\equiv \frac{1}{L} \int_{l=0}^{L} Z_m(l) dl \\
&= \frac{1}{L} Z_{e,i} 10^{-0.2K_i L} \int_{l=0}^{L} 10^{-0.2k_i l} dr \\
&= Z_{e,i} 10^{-0.2K_i L} \frac{1-10^{-0.2k_i L}}{0.2(\ln 10)k_i L}.
\end{aligned} \tag{9}
$$

If $0.1(\ln 10) k_i L \ll 1$,

$$
\begin{aligned}
\frac{1-10^{-0.2k_i L}}{0.2(\ln 10)k_i L} &= 10^{-0.1k_i L} \frac{e^{0.1(\ln 10)k_i L} - e^{-0.1(\ln 10)k_i L}}{0.2(\ln 10)k_i L} \\
&\approx 10^{-0.1k_i L}.
\end{aligned} \tag{10}
$$

From Eqs. (9) and (10),

$$
\mathrm{dB}Z_{m,i} = \mathrm{dB}Z_{e,i} - 2K_i L - k_i L, \tag{11}
$$

where $\mathrm{dB}X$ means $10 \log_{10} X$. $2K_i L$ is attenuation caused by precipitation particles above range bin i. $k_i L$ is attenuation caused by precipitation particles at range bin i.

Without the approximation of Eq. (10), Eq. (11) is replaced by

$$
\mathrm{dB}Z_{m,i} = \mathrm{dB}Z_{e,i} - 2K_i L - \gamma k_i L, \tag{12}
$$

where γ satisfies

$$
\frac{1-10^{-0.2k_i L}}{0.2(\ln 10)k_i L} = 10^{-0.1\gamma k_i L}. \tag{13}
$$

Here, γ is a decreasing function of k_i and $0 < \gamma < 1$.

In the rest of this paper, the subscript i is omitted for simplicity.

2.3 Constraints

There are $2n$ unknown parameters (D_m and N_w at n range bins), whereas the number of measurements (Z_m at n range bins and $\mathrm{PIA_{SRT}}$) in the single-frequency and dual-frequency algorithms are $n + 1$ and $2n + 2$, respectively. In the single-frequency algorithm, except for the case of $n = 1$, the number of unknown parameters is larger than the number of measurements. Thus, additional equations are needed to constrain unknown parameters.

However, constraints need not be expressed directly in terms of N_w and D_m. Because Z_e, R, and k are functions of N_w and D_m, these values can also be used for constraints. Although the PR algorithm uses a $k-Z_e$ relation, the DPR algorithms assume an $R-D_m$ relation

in the following form

$$
R = g(D_m) \tag{14}
$$

where g is derived in Section 4.

2.4 Forward retrieval method

Here, Eqs. (4)–(6), (12), and (14) are given. The forward retrieval method determines unknown parameters sequentially from range bin 1 to range bin n as follows.

a. Range bin 1

At range bin 1, $K = 0$ from Eq. (8). Thus, Eq. (12) becomes,

$$
\mathrm{dB}Z_m = \mathrm{dB}Z_e - \gamma kL. \tag{15}
$$

From Eqs. (6) and (14),

$$
N_w = \frac{g(D_m)}{f_R(D_m)c(h)}. \tag{16}
$$

Substituting Eqs. (4), (5), and (16) into Eq. (15) yields,

$$
\begin{aligned}
\mathrm{dB}Z_m = {} & 10\log_{10}\left[\frac{g(D_m)f_z(D_m)}{f_R(D_m)c(h)}\right] \\
& - \gamma(D_m)\frac{g(D_m)f_k(D_m)}{f_R(D_m)c(h)}L.
\end{aligned} \tag{17}
$$

From Eqs. (5), (13), and (16), γ is a function of D_m.

D_m is selected to satisfy Eq. (17), and N_w is calculated using Eq. (16). Once D_m and N_w are given, Z_e, k, and R can be calculated using Eqs. (4), (5), and (6), respectively.

b. Other range bins

Z_f is defined by

$$
\mathrm{dB}Z_f \equiv \mathrm{dB}Z_e - \gamma kL. \tag{18}
$$

From Eqs. (12) and (18),

$$
\mathrm{dB}Z_f = \mathrm{dB}Z_m + 2KL. \tag{19}
$$

Because K is determined at the range bins above the current range bin, the value is known from the forward retrieval method. Therefore, Z_f can be calculated using Eq. (19).

Substituting Eqs. (4), (5), and (16) into Eq. (18) yields,

$$
\begin{aligned}
\mathrm{dB}Z_f = {} & 10\log_{10}\left[\frac{g(D_m)f_z(D_m)}{f_R(D_m)c(h)}\right] \\
& - \gamma(D_m)\frac{g(D_m)f_k(D_m)}{f_R(D_m)c(h)}L,
\end{aligned} \tag{20}
$$

where D_m is selected to satisfy Eq. (20). Once D_m is obtained, N_w, Z_e, k, and R can be calculated.

2.5 Maximum likelihood method

After k is determined for range bins 1 to n using the forward retrieval method, PIA is calculated as

$$\text{PIA}_g \equiv \sum_{i=1}^{n} 2k_i L. \tag{21}$$

Because the function g is used in the forward retrieval method, the subscript g is used to identify the source of this PIA.

On the other hand, PIA_{SRT} can be expressed as

$$\text{PIA}_{\text{SRT}} \equiv \text{dB}\sigma_e^0 - \text{dB}\sigma_m^0, \tag{22}$$

where σ_m^0 is the measured surface backscattering cross section with precipitation and σ_e^0 is the surface backscattering cross section without precipitation.

If PIA_{SRT} is correct, the function g should be modified so PIA_g equals PIA_{SRT}. However, SRT is not perfect, thus g is modified following the maximum likelihood method.

3. Scattering table

In this section, f_z, f_k, and f_R are derived based on precipitation particle characteristics.

3.1 Liquid precipitation

At and below the bottom of the BB (or 0°C height if no BB exists), precipitation particles are in a liquid phase and the liquid precipitation particles are assumed to be spherical in shape. The temperature of the particle is set to T. Based on Mie scattering theory, backscattering cross section σ_b $(D; \lambda, T)$ (mm^2) and extinction cross section σ_e $(D; \lambda, T)$ (mm^2) can be calculated for a particle with drop size diameter D and temperature T, where λ is the wave length of the microwave (mm).

Here, Z_e (mm^6 m^{-3}) can be calculated as

$$Z_e = \frac{\lambda^4}{\pi^5 |K_w(\lambda)|^2} \int_{D=0}^{\infty} \sigma_b(D; \lambda, T) N(D) \, dD$$
$$= N_w \frac{\lambda^4}{\pi^5 |K_w(\lambda)|^2} \int_{D=0}^{\infty} \sigma_b(D; \lambda, T) f(D; D_m) \, dD, \tag{23}$$

where $\quad K_w(\lambda) \equiv \dfrac{n_{w0}(\lambda)^2 - 1}{n_{w0}(\lambda)^2 + 2}, \tag{24}$

where $n_{w0}(\lambda)$ is the refractive index for liquid water at 0°C. The value of $|K_w(\lambda)|^2$ is 0.9255 for KuPR and 0.8989 for KaPR. From Eqs. (4) and (23),

$$f_Z(D_m) = \frac{\lambda^4}{\pi^5 |K_w(\lambda)|^2} \int_{D=0}^{\infty} \sigma_b(D; \lambda, T) f(D; D_m) \, dD. \tag{25}$$

Here, k (dB km^{-1}) can be expressed as

$$k = \frac{0.01}{\ln 10} \int_{D=0}^{\infty} \sigma_e(D; \lambda, T) N(D) \, dD$$
$$= N_w \frac{0.01}{\ln 10} \int_{D=0}^{\infty} \sigma_e(D; \lambda, T) f(D; D_m) \, dD. \tag{26}$$

From Eqs. (5) and (26),

$$f_k(D_m) = \frac{0.01}{\ln 10} \int_{D=0}^{\infty} \sigma_e(D; \lambda, T) f(D; D_m) \, dD. \tag{27}$$

The value of R (mm h^{-1}) is calculated as

$$R = 0.6\pi \times 10^{-3} \int_{D=0}^{\infty} V(D) c(h) D^3 N(D) \, dD$$
$$= N_w \times 0.6\pi \times 10^{-3} \int_{D=0}^{\infty} V(D) c(h) D^3 f(D; D_m) \, dD, \tag{28}$$

where $V(D)$ is the fall speed (m s^{-1}) of a liquid precipitation particle with drop size diameter D at $h = 0$. From Eqs. (6) and (28),

$$f_R(D_m) = 0.6\pi \times 10^{-3} \int_{D=0}^{\infty} V(D) D^3 f(D; D_m) \, dD. \tag{29}$$

According to Atlas and Ulbrich (1977), $V(D)$ is assumed to be

$$V(D) = 3.78 D^{0.67}. \tag{30}$$

Substituting Eqs. (2) and (30) into Eq. (29) yields,

$$f_R(D_m) = 0.6\pi \times 10^{-3} \times 3.78$$
$$\times \frac{6\Gamma(\mu + 4.67)}{4^4 (\mu + 4)^{0.67} \Gamma(\mu + 4)} D_m^{4.67}. \tag{31}$$

Because $\mu = 3$, Eq. (31) becomes

$$f_R(D_m) = 0.1644 \times 10^{-3} \times D_m^{4.67}. \tag{32}$$

3.2 Mixed-phase precipitation

Above the bottom of the BB (or 0°C height if no BB exists), precipitation particles are a mixture of liquid water, ice, and air, and thus are known as mixed-phase particles. The shape of a mixed-phase particle is assumed to be spherical and its density is assumed to be dependent on T or the relative position to the BB, but independent of particle size. Following Thurai

Table 1.   Parameters of precipitation particles at different altitudes.

Without BB	With BB	phase	T (°C)	P_w	P_i	ρ_s (g cm^{-3})	U
Above 0°C height	Above BB	50	−50	0.000	0.109	0.100	2.0
		$T + 100$	$-50 < T < 0$		(not explicitly given)		
	Top of BB	100	0	0.017	0.123	0.130	3.4
	Between top and peak of BB	125	0	0.044	0.180	0.210	8.7
	Peak of BB	150	0	0.170	0.263	0.412	140
	Between peak and bottom of BB	175	0	0.380	0.257	0.616	140
0°C height	Bottom of BB	200	0	1.000	0.000	1.000	n/a
Below 0°C height	Below BB	$T + 200$	$0 < T \leq 50$	1.000	0.000	1.000	n/a

et al. (2001), the particle density and other parameters of mixed-phase particles are set as follows.

If a BB exists, the volumetric ratio of liquid water, P_w, the volumetric ratio of solid ice, P_i, and particle mass density, ρ_s (g cm^{-3}) are prescribed at $T = -50$°C (phase = 50) and at several altitudes relative to the BB: the top of the BB (phase = 100), the peak of the BB (phase = 150), the bottom of the BB (phase = 200), between the top and the peak of the BB (phase = 125), and between the peak and the bottom of the BB (phase = 175). If no BB exists, the parameters are prescribed at $T = -50$°C (phase = 50) and $T = 0$°C (phase = 200). The refractive index, n_s, of the mixed-phase particle can be expressed as

$$\frac{n_s^2 - 1}{n_s^2 + U} = P_w \frac{n_w(T,\lambda)^2 - 1}{n_w(T,\lambda)^2 + U} + P_i \frac{n_i(T,\lambda)^2 - 1}{n_i(T,\lambda)^2 + U}, \quad (33)$$

where $n_w(T,\lambda)$ and $n_i(T,\lambda)$ are the refractive indices of liquid water and solid ice, respectively, at temperature T and wavelength λ. The values of P_w, P_i, ρ_s, and U are listed in Table 1.

Based on Mie scattering theory, backscattering cross section $\sigma_b(D_s; \lambda, T, n_s)$ and extinction cross section $\sigma_e(D_s; \lambda, T, n_s)$ can be calculated for a particle with drop size diameter D_s, temperature T, and refractive index n_s.

According to Magono and Nakamura (1965), the fall speed V_s (m s^{-1}) of a mixed-phase particle at $h = 0$, if $0.05 \leq \rho_s$ (g cm^{-3}) ≤ 0.3, is

$$V_s(D_s; \rho_s) = 8.8 \times (0.1 D_s \rho_s)^{0.5}. \quad (34)$$

If $\rho_s > 0.3$ g cm^{-3},

$$V_s(D_s; \rho_s) = \frac{(\rho_s^{1/3} - 0.3^{1/3})}{(1.0 - 0.3^{1/3})}[V(D) - V_{s,0.3}(D_s)] + V_{s,0.3}(D_s), \quad (35)$$

where $V_{s,0.3}(D_s)$ is V_s calculated by Eq. (34), with $\rho_s =$

0.3 g cm^{-3}, and D is the drop size diameter after the particle is melted, and can be calculated as

$$D = \rho_s^{1/3} D_s. \quad (36)$$

It is assumed that if mixed-phase particles are melted in place (at the same h), the DSD of melted particles would be given by Eq. (1). This assumption can be expressed as

$$N(D)V(D)dD = N_s(D_s)V_s(D_s; \rho_s)dD_s, \quad (37)$$

where $N_s(D_s)$ is the DSD for mixed-phase precipitation. N_w and D_m of $N(D)$ are used for the DSD parameters of mixed-phase precipitation.

Z_e can then be derived as

$$\begin{aligned} Z_e &= \frac{\lambda^4}{\pi^5 |K_w(\lambda)|^2} \int_{D_s=0}^{\infty} \sigma_b(D_s; \lambda, T, n_s) N_s(D_s) dD_s \\ &= N_w \frac{\lambda^4}{\pi^5 |K_w(\lambda)|^2} \\ &\quad \times \int_{D=0}^{\infty} \sigma_b(D_s; \lambda, T, n_s) \frac{V(D)}{V_s(D_s; \rho_s)} f(D; D_m) dD. \end{aligned}$$
$$(38)$$

From Eqs. (4) and (38),

$$\begin{aligned} f_Z(D_m) &= \frac{\lambda^4}{\pi^5 |K_w(\lambda)|^2} \int_{D=0}^{\infty} \sigma_b(D_s; \lambda, T, n_s) \\ &\quad \times \frac{V(D)}{V_s(D_s; \rho_s)} f(D; D_m) dD. \end{aligned}$$
$$(39)$$

Here, k is derived as

$$\begin{aligned} k &= \frac{0.01}{\ln 10} \int_{D_s=0}^{\infty} \sigma_e(D_s; \lambda, T, n_s) N_s(D_s) dD_s \\ &= N_w \frac{0.01}{\ln 10} \int_{D=0}^{\infty} \sigma_e(D_s; \lambda, T, n_s) \\ &\quad \times \frac{V(D)}{V_s(D_s; \rho_s)} f(D; D_m) dD. \end{aligned}$$
$$(40)$$

From Eqs. (5) and (40),

$$f_k(D_m) = \frac{0.01}{\ln 10} \int_{D=0}^{\infty} \sigma_e(D_s; \lambda, T, n_s)$$
$$\times \frac{V(D)}{V_s(D_s; \rho_s)} f(D; D_m) dD. \quad (41)$$

Here, R is derived as

$$R = 0.6\pi \times 10^{-3} \int_{D_s=0}^{\infty} V_s(D_s) c(h) \rho_s D_s^3 N_s(D_s) dD_s$$
$$= N_w \times 0.6\pi \times 10^{-3} \int_{D=0}^{\infty} V(D) c(h) D^3 f(D; D_m) dD. \quad (42)$$

From Eqs. (6) and (42),

$$f_R(D_m) = 0.6\pi \times 10^{-3} \int_{D=0}^{\infty} V(D) D^3 f(D; D_m) dD, \quad (43)$$

which is the same as Eq. (29).

Although many studies have investigated the scattering properties of non-liquid precipitation particles with more complicated and realistic simulations (e.g., Liu 2004; Liao et al. 2013, 2016, 2020; Nowell et al. 2013; Kuo et al. 2016), the DPR algorithms apply a simple model assuming spherical particles with fixed density. Liao et al. (2013) compared the backscattering and extinction cross sections of non-spherical particles calculated using a discrete dipole approximation (DDA) with those of mass-equivalent spherical particles with a fixed density calculated by Mie theory. For Ku-band and Ka-band frequencies, the results agreed well when particle size is less than 2.5 mm. If the particle density is assumed to depend on particle size, density becomes lower for larger particles, which can lead to disagreement with DDA calculations. According to Liao et al. (2013), particle density for the Ka-band is recommended to be 0.2 g cm^{-3} or higher. Kuo et al. (2016) performed similar tests and concluded that the fixed density between 0.1 g cm^{-3} and 0.3 g cm^{-3} produces backscattering and extinction cross sections similar to those calculated by DDA for Ku-band and Ka-band frequencies. The use of a simple scattering model in the DPR algorithms, with an assumed fixed density of 0.1 g cm^{-3} or higher, is thus acceptable based on the previous studies.

3.3 Scattering table

The values of f_z (for KuPR and KaPR), f_k (for KuPR and KaPR), and f_R are calculated for a combination of D_m (0.1−5.0 mm with a step of 0.001 mm) and phase (50−99, 100*, 125*, 150*, 175*, and 200−250; *

with BB), and these values are stored in the scattering table. For phases equal to 50, 100, 125, 150, and 175, f_z and f_k are calculated using Eqs. (39) and (41). For phases between 200 and 250 (i.e., liquid phase precipitation with T = phase − 200), f_z and f_k are calculated using Eqs. (25) and (27). For phases between 51 and 99 (i.e., mixed-phase precipitation with T = phase − 100), f_Z and f_k are interpolated between the phases at 50 and 100 (50 and 200 if no BB exists) by assuming that dBf_Z and f_k are linear functions of T. Values of dBf_z and dBf_k are shown for different phase and D_m values in Fig. 4 (with BB) and Fig. 5 (without BB). If $T < -50°C$, the scattering table for phase 50 is used. f_R does not depend on phase, and thus is calculated using Eq. (32).

4. $R-D_m$ relation

In this section, the $R-D_m$ relation, or $g(D_m)$, is derived.

4.1 Reasons why the $R-D_m$ relation is used in DPR algorithms

The PR algorithm used the $k-Z_e$ relation as a DSD constraint. Kozu et al. (2009a, b) summarized precipitation measurements in the tropics and obtained a $Z-R$ relation in the standard form as

$$Z = aR^b, \quad (44)$$

where Z is the radar reflectivity factor (mm^6 m^{-3}) and $a = 298.84$ and $b = 1.38$ for stratiform precipitation and $a = 184.20$ and $b = 1.43$ for convective precipitation. Kozu et al. (2009b) derived the $k-Z_e$ relation from the $Z-R$ relation as

$$k = \alpha Z_e^{\beta}, \quad (45)$$

where α and β are constants. In the PR algorithm (version 6), $\alpha = 0.000282$ and $\beta = 0.7923$ for stratiform precipitation and $\alpha = 0.000411$ and $\beta = 0.7713$ for convective precipitation in the case of liquid-phase precipitation at 0°C.

Using a $k-Z_e$ relation and the Hitschfeld-Bordan method (Hitschfeld and Bordan 1954), the PR algorithm can derive a profile of Z_e from the profile of Z_m without a scattering table. The $k-Z_e$ relation is applicable to the KuPR; however, no $k-Z_e$ relation in the form of Eq. (45) is suitable for the KaPR as will be explained in Section 4.4. Therefore, the DPR algorithms do not use the $k-Z_e$ relation, but instead use the $R-D_m$ relation.
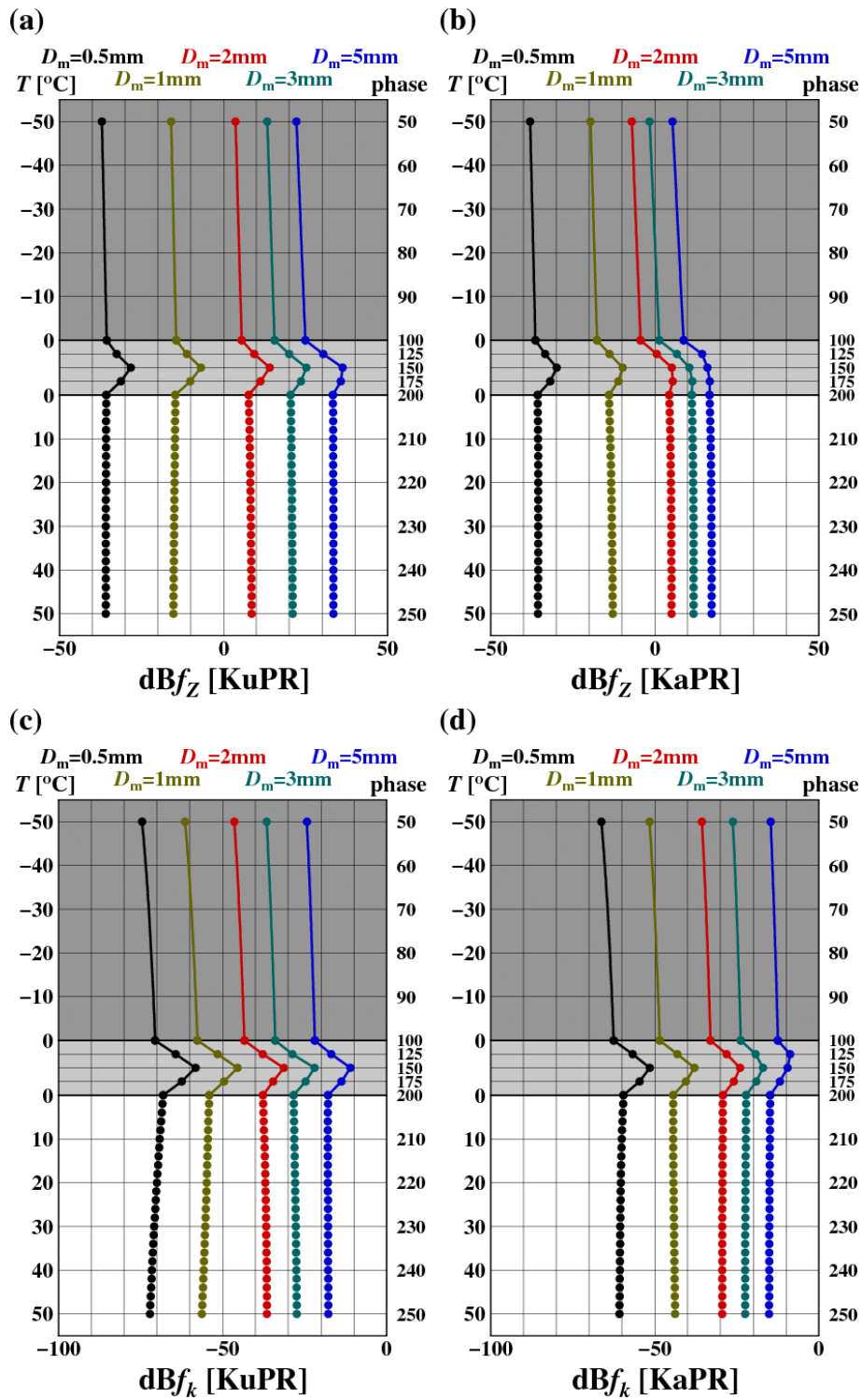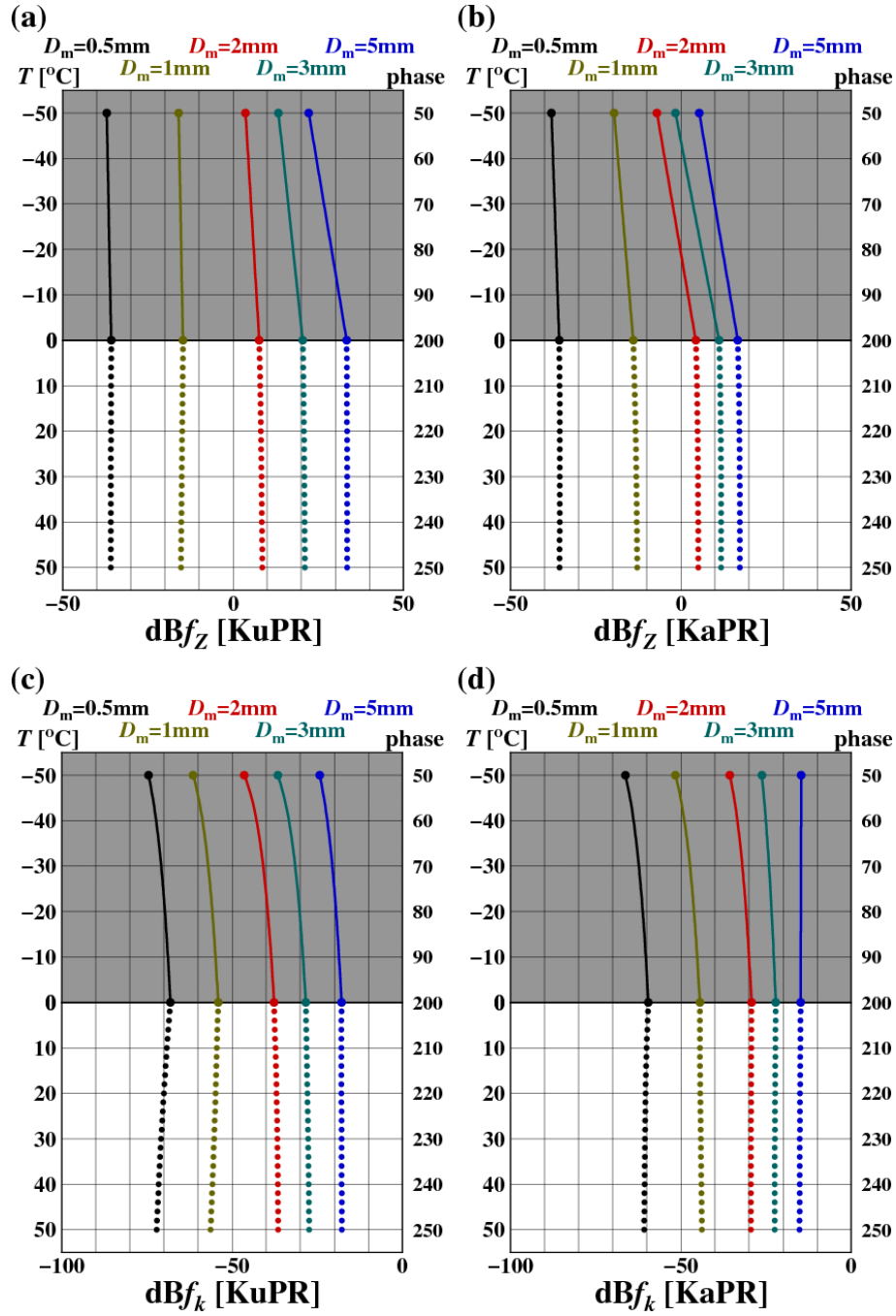
Fig. 4.   Samples of a scattering table for pixels with a bright band. (a) and (b) show dB$f_z(D_m)$ and (c) and (d) are for dB$f_k(D_m)$. (a) and (c) are for KuPR and (b) and (d) are for KaPR.

(a)

(b)

(c)

(d)

Fig. 5. Samples of a scattering table for pixels without a bright band. (a) and (b) show dB$f_z(D_m)$ and (c) and (d) are for dB$f_k(D_m)$. (a) and (c) are for KuPR and (b) and (d) are for KaPR.

4.2 Derivation of the R−D_m relation

The R−D_m relation is derived below.

From the Rayleigh approximation, Z is defined as

$$Z \equiv \int_{D=0}^{\infty} D^6 N(D) \, dD, \tag{46}$$
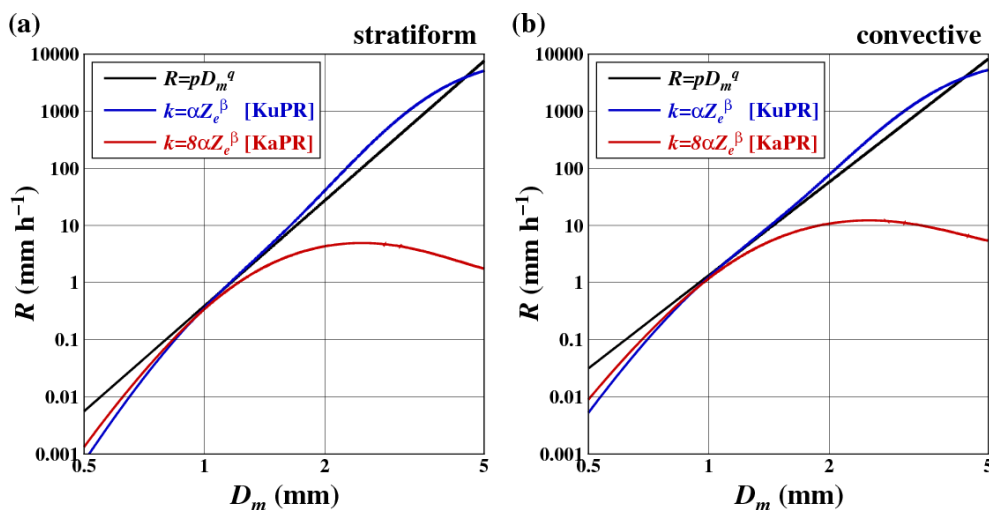
Substituting Eqs. (1) and (2) into Eq. (46) yields,

Fig. 6.   Comparison of $R-D_m$ relation and $k-Z_e$ relations. (a) represents stratiform precipitation and (b) represents convective precipitation.

$$Z = N_w \int_{D=0}^{\infty} D^6 f(D; D_m) \, dD$$
$$= N_w \frac{6(\mu+6)(\mu+5)}{4^4(\mu+4)^2} D_m^7. \tag{47}$$

As $\mu = 3$,

$$Z = 0.034439 \times N_w D_m^7. \tag{48}$$

From Eqs. (6) and (32),

$$R = 0.1644 \times 10^{-3} \times N_w D_m^{4.67}, \tag{49}$$

where $c(h) = 1$ is assumed.

Substituting Eqs. (48) and (49) into Eq. (44) yields,

$$R = \left(\frac{0.034439}{a \times 0.1644 \times 10^{-3}} \right)^{\frac{1}{b-1}} D_m^{\frac{2.33}{b-1}}. \tag{50}$$

Therefore, $g(D_m)$ is

$$g(D_m) = p D_m^q, \tag{51}$$

where $\quad p = \left(\frac{0.034439}{a \times 0.1644 \times 10^{-3}} \right)^{\frac{1}{b-1}}, \tag{52}$

and $\quad q = \frac{2.33}{b-1}. \tag{53}$

Substituting a and b from Eq. (44) into Eqs. (52) and (53) yields $p = 0.392$ and $q = 6.131$ for stratiform precipitation and $p = 1.348$ and $q = 5.418$ for convective precipitation.

4.3   Comparison of $k-Z_e$ relation and $R-D_m$ relation

According to Kozu et al. (2009b), the $k-Z_e$ relation was derived by regression analysis from the $Z-R$ relation. Thus, the $k-Z_e$ relation and $R-D_m$ relation are not completely the same. The two relations are compared below.

Substituting Eqs. (4) and (5) into Eq. (45) yields,

$$N_w f_k(D_m) = \alpha [N_w f_z(D_m)]^\beta. \tag{54}$$

From Eq. (54), N_w is given as

$$N_w = \left\{ \frac{\alpha [f_z(D_m)]^\beta}{f_k(D_m)} \right\}^{\frac{1}{1-\beta}}. \tag{55}$$

Substituting Eq. (55) into Eq. (6) yields,

$$R = \left\{ \frac{\alpha [f_z(D_m)]^\beta}{f_k(D_m)} \right\}^{\frac{1}{1-\beta}} f_R(D_m) c(h). \tag{56}$$

For liquid-phase precipitation with $T = 0°C$, α and β (as used in the PR standard algorithm), f_Z (for KuPR), f_k (for KuPR), f_R, and $c(h) = 1$ are substituted into Eq. (56), then the relation between R and D_m can be numerically obtained. This relation is represented by the blue curve in Fig. 6. α and β for stratiform precipitation are used in Fig. 6a and those for convective precipitation are used in Fig. 6b. The $R-D_m$ relation in Eq. (51) is shown by the black line in each figure. As both axes in Fig. 6 are on a logarithmic scale, the $R-D_m$ relation is a straight line. The $k-Z_e$ and $R-D_m$ relations are generally close to each other when 0.1 mm h$^{-1} < R < 100$ mm h^{-1}.

4.4 Investigation of the $k−Z_e$ relation for KaPR

Here we attempt to apply the $k−Z_e$ relation to the KaPR. Because KaPR has stronger attenuation than PR, the α value for KaPR is eight times larger than the α used in the PR standard algorithm. Additionally, β is set to be the same as that of PR. For liquid-phase precipitation with $T = 0°C$, α and β (as explained above), f_Z (for KaPR), f_k (for KaPR), f_R, and $c(h) = 1$ are substituted into Eq. (56). The numerical relation between R and D_m is then obtained as represented by the red curve in Fig. 6. The $k−Z_e$ relation for KaPR is notably different from the $R−D_m$ relation. If α changes, the red curve moves upward or downward; however, the shape remains the same. The red curve has a local maximum at approximately $D_m = 2.5$ mm. It seems unnatural that R is a decreasing function of D_m when D_m is larger than 2.5 mm. If β changes, the red curve is never close to the $R−D_m$ relation. Therefore, the $k−Z_e$ relation in the form of Eq. (45) is not appropriate for KaPR.

4.5 $R−D_m$ relation for mixed-phase precipitation

As in Section 3.2, it is assumed that Eq. (37) holds if mixed-phase particles are melted in place (at the same h), thus the N_w and D_m values of $N(D)$ are used for the DSD parameters of mixed-phase precipitation. Note that $f_R (D_m)$ does not depend on phase. Because D_m and R do not change after mixed-phase particles melt, the same $R−D_m$ relation can be used for mixed-phase precipitation.

4.6 Modification of $R−D_m$ relation

As noted in Section 2.5, the $R−D_m$ relation must be modified when PIA_{SRT} is available. In the PR standard algorithm, the $k−Z_e$ relation is modified by adjustment factor ε as

$$k = \varepsilon \alpha Z_e^{\beta}. \tag{57}$$

From Eqs. (4)−(6) and (57),

$$R = \left\{ \frac{\varepsilon \alpha [f_z(D_m)]^{\beta}}{f_k(D_m)} \right\}^{\frac{1}{1-\beta}} f_R(D_m) c(h). \tag{58}$$

A comparison of Eqs. (56) and (58) shows that the adjustment factor for the $R−D_m$ relation is $\varepsilon^{1/(1-\beta)}$. Thus, Eq. (51) then becomes

$$g(D_m) = \varepsilon^r p D_m^q, \tag{59}$$

where $r = \dfrac{1}{1-\beta}. \tag{60}$

Here $r = 4.815$ for stratiform precipitation and $r =$

4.373 for convective precipitation.

5. NUBF correction

This section explains NUBF correction. NUBF was not considered in the previous sections, thus some equations must be modified.

5.1 Assumptions about NUBF

A radar beam (denoted by B) is the combination of sub-beams with very narrow beam widths. As in Eq. (1), DSD in a sub-beam (denoted by S) is assumed as

$$N_S(D) = N_{w,S} f(D; D_{m,S}), \tag{61}$$

where $D_{m,S}$ and $N_{w,S}$ are DSD parameters and f is the same as in Eq. (2). The subscript S denotes sub-beam S. Here, $D_{m,s}$ and $N_{w,s}$ are assumed to be

$$D_{m,S} = D_{m,B}, \tag{62}$$

and $N_{w,S} = sN_{w,B}, \tag{63}$

where s depends on S but not on range. $D_{m,B}$ and $N_{w,B}$ are constants for the beam B.

The probability density function of s can thus be assumed to be

$$p_0(s) = \frac{t^t}{\Gamma(t)} s^{t-1} \exp(-ts), \tag{64}$$

where t is a probability distribution parameter that should be positive. The mean of s is calculated as

$$\int_{s=0}^{\infty} s p_0(s) ds = \frac{t^t}{\Gamma(t)} \int_{s=0}^{\infty} s^t \exp(-ts) ds$$
$$= \frac{t^t}{\Gamma(t)} \frac{\Gamma(t+1)}{t^{t+1}} = 1, \tag{65}$$

and the variance of s is calculated as

$$\int_{s=0}^{\infty} (s-1)^2 p_0(s) ds = \frac{t^t}{\Gamma(t)} \int_{s=0}^{\infty} s^{t+1} \exp(-ts) ds - 1$$
$$= \frac{t^t}{\Gamma(t)} \frac{\Gamma(t+2)}{t^{t+2}} - 1 = t^{-1}. \tag{66}$$

Because $N_{w,S}$ is proportional to s, the average of $N_{w,S}$ in beam B is $N_{w,B}$. Because $D_{m,S}$ is constant, it is evident that the average of $D_{m,S}$ in the beam B is $D_{m,B}$.

5.2 Equations

In sub-beam S, effective radar reflectivity factor $Z_{e,S}$, specific attenuation k_S, and precipitation rate R_S can be expressed as

$$Z_{e,S} = N_{w,S} f_z(D_{m,S}) = sN_{w,B} f_z(D_{m,B}), \tag{67}$$

$$k_S = N_{w,S} f_k(D_{m,S}) = s N_{w,B} f_k(D_{m,B}), \tag{68}$$

and

$$R_S = N_{w,S} f_R(D_{m,S}) c(h) = s N_{w,B} f_R(D_{m,B}) c(h). \tag{69}$$

Taking the averages of Eqs. (67)–(69) in beam B yields,

$$Z_{e,B} = N_{w,B} f_z(D_{m,B}), \tag{70}$$

$$k_B = N_{w,B} f_k(D_{m,B}), \tag{71}$$

and $$R_B = N_{w,B} f_R(D_{m,B}) c(h), \tag{72}$$

where $Z_{e,B}$, k_B, and R_B are the average values in the beam B. These equations mean that the scattering table or Eqs. (4)–(6) can be used for the average values in uniform and non-uniform cases.

The $R-D_m$ relation is assumed to hold for the average values so that

$$R_B = g(D_{m,B}), \tag{73}$$

where g is the same as the uniform case described in Eq. (14); however, $R_S = g(D_{m,S})$ in any sub-beam is not guaranteed.

In the rest of this paper, the subscript B will be omitted so that variables without the subscript S mean the average values of the beam B.

5.3   Effects of NUBF on forward retrieval method

In sub-beam S, the measured radar reflectivity factor, $Z_{m,S}$, at range bin i is given by

$$\mathrm{dB}Z_{m,S} = \mathrm{dB}Z_{e,S} - 2K_S L - \gamma_S k_S L, \tag{74}$$

where $$K_S \equiv \sum_{j=1}^{i-1} k_{j,S} = \sum_{j=1}^{i-1} (s k_j) = sK, \tag{75}$$

and $$\frac{1 - 10^{-0.2 k_S L}}{0.2 (\ln 10) k_S L} = 10^{-0.1 \gamma_S k_S L}. \tag{76}$$

For simplicity, γ_S is replaced by γ in Eq. (13), so that Eq. (74) becomes

$$\mathrm{dB}Z_{m,S} = \mathrm{dB}Z_{e,S} - 2K_S L - \gamma k_S L. \tag{77}$$

Then the average of $Z_{m,S}$ in the beam B can be calculated as

$$Z_m = \int_{S \in B} Z_{m,S} dS = \int_{S \in B} Z_{e,S} 10^{-0.1(2K_S + \gamma k_S)L} dS$$
$$= Z_e [1 + 0.1(\ln 10) t^{-1}(2K + \gamma k) L]^{-(t+1)}. \tag{78}$$

Eq. (78) is then rewritten as

$$\mathrm{dB}Z_m = \mathrm{dB}Z_e - 10(t+1)$$
$$\times \log_{10}[1 + 0.1(\ln 10) t^{-1}(2K + \gamma k) L]. \tag{79}$$

$Z_{f,S}$ is defined as

$$\mathrm{dB}Z_{f,S} \equiv \mathrm{dB}Z_{e,S} - \gamma k_S L. \tag{80}$$

As in Eq. (77), γ is used instead of γ_S for simplicity.

The average of $Z_{f,S}$ in the beam B is

$$Z_f = \int_{S \in B} Z_{f,S} dS = \int_{S \in B} Z_{e,S} 10^{-0.1 \gamma k_S L} dS$$
$$= Z_e [1 + 0.1(\ln 10) t^{-1} \gamma k L]^{-(t+1)}. \tag{81}$$

Eq. (81) can be rewritten as

$$\mathrm{dB}Z_f = \mathrm{dB}Z_e - 10(t+1) \log_{10}[1 + 0.1(\ln 10) t^{-1} \gamma k L]. \tag{82}$$

From Eqs. (79) and (82),

$$\mathrm{dB}Z_f = \mathrm{dB}Z_m + 10(t+1)$$
$$\times \log_{10}\left[\frac{1 + 0.1(\ln 10) t^{-1}(2K + \gamma k) L}{1 + 0.1(\ln 10) t^{-1} \gamma k L}\right], \tag{83}$$

and Eq. (83) can be approximated as

$$\mathrm{dB}Z_f = \mathrm{dB}Z_m + 10(t+1) \log_{10}[1 + 0.2(\ln 10) t^{-1} K L]. \tag{84}$$

In the forward retrieval method, Eqs. (12), (18), and (19) are used in the uniform case; however, in non-uniform cases they are replaced by Eqs. (79), (82), and (84), respectively.

5.4   Effects of NUBF on SRT

In sub-beam S, $\mathrm{PIA}_{g,S}$ is defined as

$$\mathrm{PIA}_{g,S} \equiv \sum_{i=1}^{n} 2 k_{i,S} L. \tag{85}$$

From Eqs. (21), (68), and (71),

$$\mathrm{PIA}_{g,S} = \sum_{i=1}^{n} 2(s k_i) L = s \mathrm{PIA}_g. \tag{86}$$

Thus, the average of $\mathrm{PIA}_{g,S}$ in beam B is PIA_g.

The measured surface backscattering cross section in sub-beam S is denoted by $\sigma_{m,S}^0$. The surface backscattering cross section without precipitation in sub-beam S is denoted by $\sigma_{e,S}^0$, and is expressed as

$$\mathrm{dB}\sigma_{e,S}^0 = \mathrm{dB}\sigma_{m,S}^0 + \mathrm{PIA}_{g,S}. \tag{87}$$

The surface is assumed to be uniform, or $\sigma_{e,S}^0$ is assumed to be constant in beam B, and is rewritten as σ_e^0. Therefore,

$$\sigma^0_{m,S} = \sigma^0_e 10^{-0.1\text{PIA}_{g,S}}. \tag{88}$$

Thus, the average of $\sigma^0_{m,S}$ in beam B can be calculated as

$$\sigma^0_m = \int_{S \in B} \sigma^0_{m,S} dS = \int_{S \in B} \sigma^0_e 10^{-0.1\text{PIA}_{g,S}} dS$$

$$= \sigma^0_e [1 + 0.1(\ln 10) t^{-1} \text{PIA}_g]^{-t}. \tag{89}$$

Eq. (89) is rewritten as

$$\text{dB}\sigma^0_e - \text{dB}\sigma^0_m = \text{PIA}_{g0}, \tag{90}$$

where $\text{PIA}_{g0} \equiv 10\log_{10}[1 + 0.1(\ln 10) t^{-1} \text{PIA}_g]^t$. (91)

In non-uniform cases, PIA_{SRT} is not an estimate of PIA_g, but PIA_{g0}. In the uniform case, PIA_{g0} is the same as PIA_g. Figure 7 shows the relationship between PIA_g and PIA_{g0} for different values of t^{-1}. When $t^{-1} = 0$ or the precipitation in the pixel is uniform, $\text{PIA}_g = \text{PIA}_{g0}$. In a non-uniform case, $\text{PIA}_g > \text{PIA}_{g0}$, thus PIA_{SRT} becomes larger through the NUBF correction. To avoid overcorrection, the upper limit of t^{-1} is set to 0.25. The NUBF correction also affects the conversions from Z_f to R and Z_f to k; however, except for the case of heavy precipitation these effects are not very large.

6.   Single-frequency algorithm

This section explains the precipitation rate retrieval algorithm in the single-frequency algorithm. At precipitation pixels, DSD, R, and related variables are estimated from the storm top to the surface level. In contrast to the assumption in Section 2, ground clutter exists and precipitation and surface echoes are sometimes missing in the real case.

First, each range bin is classified into three types (as explained in Section 6.1). Next, the forward retrieval method is applied with different values of ε between 0.2 and 5.0 (as explained in Section 6.2). The results are then evaluated and the best value for ε is selected (as explained in Section 6.3). The NUBF parameter is derived from the results of the first loop and the NUBF correction is applied in the second loop (as explained in Section 6.4).

6.1   Classification of range bin types

The precipitation, main lobe, and sidelobe echoes are examined in the Preparation module. At each range bin, a determination is made as to the presence or absence of precipitation and the presence or absence of surface clutter. Next, each range bin is classified into one of three types: rain certain, rain possible, and no rain in the Solver module, based on the judgments
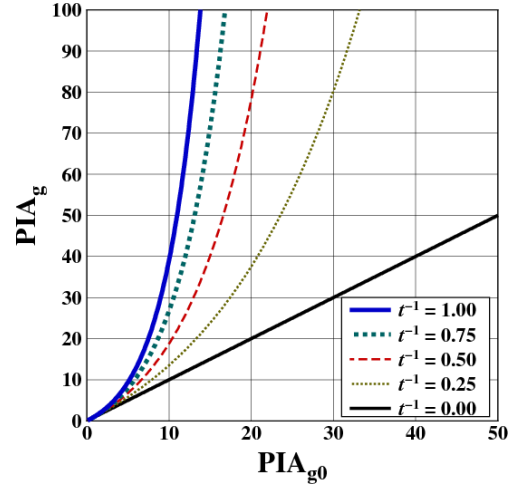

Fig. 7.   Relation between PIA_{g0} and PIA for different values of t^{-1}.

made in the Preparation module. The classification procedure is shown in Fig. 8.

Range bins above the storm top are judged to be of the no rain type. Range bins in the main lobe clutter region, which is below the clutter free bottom (CFB) and at and above the surface, are judged to be of the rain possible type. The following explanation is for range bins between the storm top and CFB. If a precipitation echo is detected and Z_m is less than 50 dBZ, the range bin is judged to be of the rain certain type. If Z_m is greater than 50 dBZ, by considering the possibility of main lobe clutter contamination, the range bin is judged to be of the rain possible type. If no precipitation echo is detected and a sidelobe echo is detected, the range bin is judged to be of the rain possible type. If neither a precipitation echo nor a sidelobe echo are detected, the range bin is judged to be of the no rain type except in the following case. If eight or more rain-certain range bins in the liquid phase exist above the range bin, the range bin is considered rain possible. This case allows for the possibility that the precipitation echo can be lost because of strong attenuation along the path.

A second screening of the data is applied for rain-possible range bins. If a rain-possible range bin, or consecutive rain-possible range bins, are located just under a no-rain range bin, those range bins are changed to no rain. Otherwise, those range bins are kept as rain possible. After the second screening, in the main lobe clutter region, which includes the surface, range bins are judged to be rain possible if the CFB is classified as rain certain or rain possible; however, they are
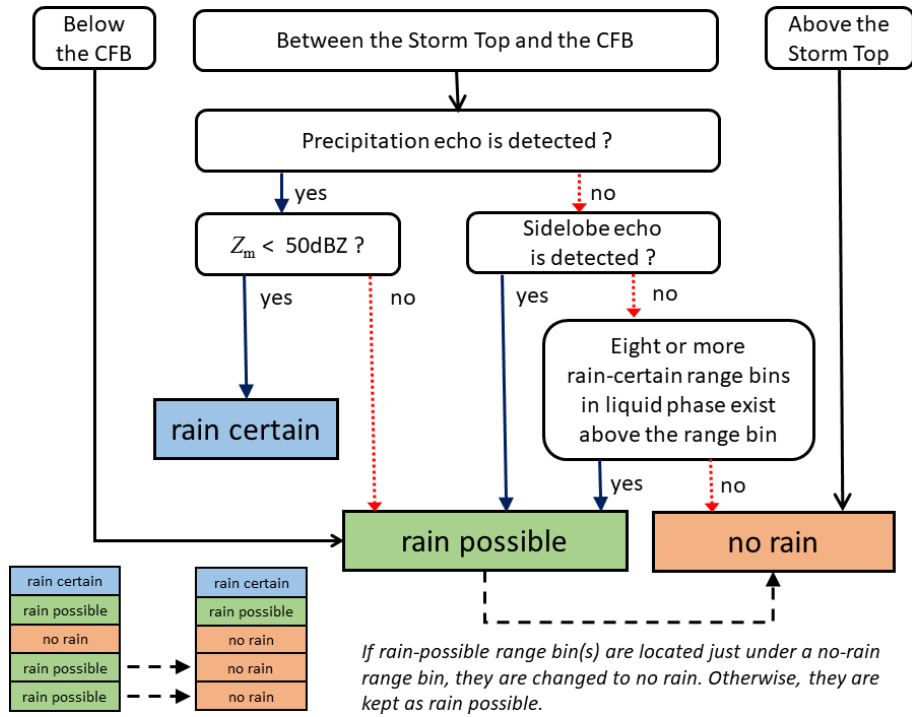
Fig. 9.   (a), (b) Relation between dBZ$_f$ and D$_m$. (c), (d) Relation between dBZ$_e$ and D$_m$. (a), (c) is for KuPR and (b), (d) is for KaPR. The solid line represents $R < 300$ mm h^{-1} and the dotted line indicates $R > 300$ mm h^{-1}. In (b), (d), $D_m > 3$ mm is shaded as the upper limit of D_m set to 3 mm in the KaPR algorithm.

D_m of the two solutions would be selected.

b.   Rain possible

At rain-possible range bins, Z_m is not available and Z_f cannot be calculated. Z_e is assumed to be vertically constant, thus Z_e is set to be the same as the value of Z_e obtained at the last range bin at which Z_m could be detected.

From Eqs. (4) and (16),

$$dBZ_e = 10\log_{10}\frac{g(D_m)f_z(D_m)}{f_R(D_m)c(h)}. \qquad (93)$$

Eq. (93) holds for both uniform and non-uniform

cases; therefore, D_m is selected using Eq. (93). Once D_m is selected, N_w is calculated using Eq. (16) and k and R are calculated using Eqs. (5) and (6).

Figures 9c and 9d show the relationship between Z_e and D_m as determined by Eq. (93) for KuPR and KaPR, respectively. Stratiform precipitation, with phase = 200 and $c(h) = 1$ is assumed and curves for ε equal to 0.2, 0.5, 1.0, 2.0, and 5.0 are drawn. The same limits of D_m and R are used as in the rain-certain case. If no solution satisfies the equation for given values of Z_e and ε, then a D_m is chosen that yields a Z_e closest to the given Z_e. Substituting Eqs. (32) and (59) into Eq. (93) yields

Fig. 10.　Sample DSD database. All surface types for June. (a) and (b) show μ_x and (c) and (d) show σ_x. (a) and (c) represent stratiform precipitation and (b) and (d) represent convective precipitation. If there are fewer than 100 samples (shown by cross symbols), the values are replaced by the global value.

$$\mathrm{dB}Z_e = 10\log_{10}\left[\frac{f_z(D_m)\varepsilon^r p}{0.1644\times10^{-3}}D_m^{\,q-4.67}\right]. \tag{94}$$
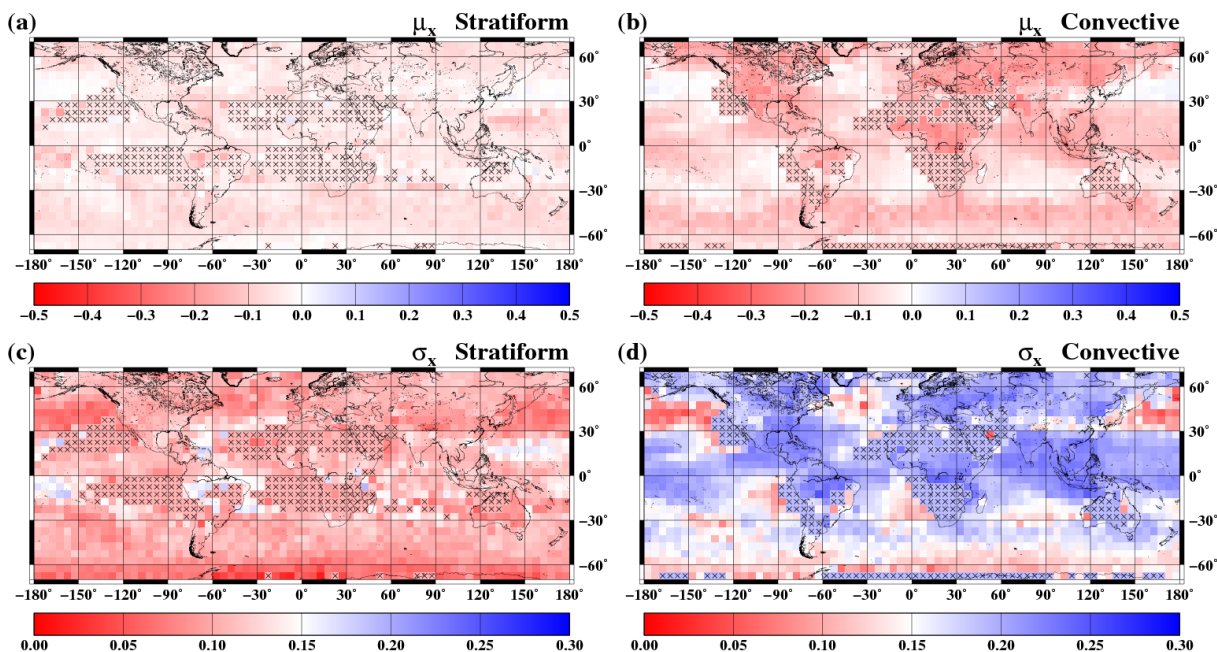
Because $q > 4.67$, $\mathrm{dB}Z_e$ is a monotonically increasing function of D_m, Eq. (93) will never have multiple solutions.

If precipitation exists in the main lobe clutter region, the above procedure is applied. Then Z_e at the CFB and Z_e at the surface become the same. Because T and h are usually different between the CFB and the surface, the precipitation rate estimates differ between the two levels.

c.　No rain

At no-rain range bins, $R = 0$ and $k = 0$, and D_m, N_w, and Z_e are set to missing or indeterminant.

6.3　Evaluation

The results of the forward retrieval method are evaluated to select the best value of ε from between 0.2 and 5.0 using the following two steps. First, ε is evaluated from 0.2 to 5.0 with an interval of 0.1 and the best value of ε is tentatively selected (denoted by ε_1). Next, ε is evaluated from $\varepsilon_1 - 0.1$ (0.2, if ε_1 is 0.2) to $\varepsilon_1 + 0.1$ (5.0, if ε_1 is 5.0) with an interval of 0.01, after

which the best value of ε is selected. At each step, the scores for E_1–E_4 are determined using multiple criteria and a value of ε is selected so that $E = E_1 + E_2 + E_3 + E_4$ is minimized.

a.　Probability distribution of ε

The probability distribution of ε is assumed to follow a log-normal distribution. In other words, $x = \log_{10}\varepsilon$ follows a normal distribution. The probability density function of x is

$$p_1(x) = \frac{1}{\sqrt{2\pi}\sigma_x}\exp\left[-\frac{(x-\mu_x)^2}{2\sigma_x^2}\right], \tag{95}$$

where μ_x and σ_x are the probability distribution parameters. In the PR standard algorithm, μ_x and σ_x depend only on precipitation type, with $\mu_x = 0.000$ and $\sigma_x = 0.146$ for stratiform precipitation and $\mu_x = 0.000$ and $\sigma_x = 0.113$ for convective precipitation. In the single-frequency algorithms for DPR, the μ_x and σ_x depend on region, month, land surface type, and precipitation type.

The values of μ_x and σ_x are stored in the DSD database. Examples are shown in Fig. 10, with global maps of μ_x and σ_x for stratiform and convective precipitation for June. The horizontal resolution is 5

degrees latitude by 5 degrees longitude, and μ_x is less than 0 for most grids. The global statistics of μ_x are approximately −0.050 for stratiform precipitation and −0.102 for convective precipitation. Convective precipitation tends to have μ_x that are smaller over land than over ocean. The global statistics of σ_x are 0.104 for stratiform precipitation and 0.191 for convective precipitation. Because the definition of ε is different for stratiform and convective precipitation, μ_x and σ_x are not directly comparable between the different precipitation types.

The values of the DSD database used in the DPR algorithms (version 06A) were derived from the results of the dual-frequency algorithm (version 05) from June 2014 to May 2016. Section 7.3 will explain that the dual-frequency algorithm has more evaluation criteria for selecting ε, whereas the KuPR algorithm mainly uses SRT, which is not very reliable for light precipitation. The DSD database attempts to convert information obtained from the dual-frequency algorithm to apply to the single-frequency algorithms. When R at the surface is between $10^{-0.5}$ and $10^{0.5}$ mm h^{-1}, $x = \log_{10}\varepsilon$ is considered a valid sample and the mean and standard deviation of x are calculated for each month as a two-year average. The 5-degree grid is then separated based on land surface type (land only, ocean only, and all surface types including coast) and precipitation type (stratiform and convective). The sample mean and standard deviation of x are estimates of μ_x and σ_x. If there are fewer than 100 samples (indicated by cross symbols in Fig. 10), those values are replaced by the global values.

b.   SRT

After the forward retrieval method calculates k over all range bins, PIA$_g$ is calculated using Eq. (21). In non-uniform cases, PIA$_{g0}$ is calculated by Eq. (91), whereas in the uniform case, PIA$_{g0}$ = PIA$_g$. PIA$_{SRT}$ may differ from PIA$_{g0}$. The conditional probability of PIA$_{SRT}$, when PIA$_{g0}$ is true, can be expressed as

$$p_2(\text{PIA}_{\text{SRT}}|\text{PIA}_{g0})$$
$$= \frac{1}{\sqrt{2\pi}\sigma_{\text{SRT}}}\exp\left[-\frac{(\text{PIA}_{\text{SRT}} - \text{PIA}_{g0})^2}{2\sigma_{\text{SRT}}^2}\right], \qquad (96)$$

where σ_{SRT} is the standard deviation of dBσ_e^0 used in SRT. The error of PIA$_{\text{SRT}}$ is assumed to follow a normal distribution.

In the maximum likelihood method, the product of p_1 and p_2 is maximized.

$$p_1(x)p_2(\text{PIA}_{\text{SRT}}|\text{PIA}_{g0})$$
$$= \frac{1}{2\pi\sigma_x\sigma_{\text{SRT}}}$$
$$\times \exp\left\{-\frac{1}{2}\left[\frac{(x-\mu_x)^2}{\sigma_x^2} + \frac{(\text{PIA}_{\text{SRT}} - \text{PIA}_{g0})^2}{\sigma_{\text{SRT}}^2}\right]\right\}, \qquad (97)$$

Eq. (97) has only one degree of freedom because PIA$_{g0}$ is a function of x and the other values are constants. To maximize the value of Eq. (97), $E_1 + E_2$ should be minimized, where

$$E_1 = \frac{(x-\mu_x)^2}{\sigma_x^2}, \qquad (98)$$

and

$$E_2 = \frac{(\text{PIA}_{\text{SRT}} - \text{PIA}_{g0})^2}{\sigma_{\text{SRT}}^2}. \qquad (99)$$

SRT is not used if its reliability is not high enough (i.e., σ_{SRT} is larger than 10 dB) or if PIA$_{\text{SRT}}$ is more than 10 times as the size of PIA as estimated using the Hitschfeld-Bordan method (PIA$_{\text{HB}}$). The latter condition is meant to avoid using significantly overestimated PIA$_{\text{SRT}}$ which may happen when surface scattering characteristics are highly variable. If SRT is not used, $E_2 = 0$.

If the surface echo is not distinguished from noise (i.e., the signal to noise ratio of the surface echo is less than 2.0), σ_m^0 is close to the noise level and may be overestimated. This suggests that PIA$_{\text{SRT}}$ is underestimated. In this situation, SRT is referred to as being "saturated". If SRT is saturated, E_2 is determined using Eq. (99) when PIA$_{g0}$ < PIA$_{\text{SRT}}$. When PIA$_{\text{SRT}}$ < PIA$_{g0}$, $E_2 = 0$.

c.   Optional criteria

Usually, $E = E_1 + E_2$ because $E_3 = E_4 = 0$; however, in some cases, E_3 and E_4 are determined as follows.

E_3 is the average of the square of ΔZ_f at the rain-certain range bins. If all rain-certain range bins have a solution for D_m, $E_3 = 0$.

E_4 is set equal to the variance of dBR (dB mm h^{-1}) at range bins in a liquid phase if SRT is either not used or is saturated. Otherwise, $E_4 = 0$.

If $E_2 = E_3 = E_4 = 0$, ε will always be 10^{μ_x}. The use of a constant ε value may lead to a divergence in the solution in the same way the solution diverges in the Hitschfeld-Bordan method. To prevent this, E_4 is used if the SRT is not used or is saturated. By using E_4, those profiles with a rapid increase in R at lower range bins may not be selected.

6.4 NUBF parameter

NUBF parameter t^{-1} must be estimated. Because t^{-1} is the variance of s, $t^{-0.5}$ is the standard deviation of s or the coefficient of variation (the ratio of the standard deviation to the mean; denoted by C_v) of other variables that are proportional to s. Because no sub-beam measurements are available, the coefficient of variation is calculated using PIA_{fin} for the eight pixels surrounding the target pixel and the target pixel itself (i.e., nine pixels). If C_v is smaller than 0.5, $t^{-1} = C_v^2$, otherwise $t^{-1} = 0.25$. To prevent overcorrection, the upper limit of t^{-1} is set to 0.25. To calculate C_v, pixels with no precipitation are excluded. If fewer than four pixels have precipitation, the NUBF correction is not applied.

7. Dual-frequency algorithm

This section explains the dual-frequency algorithm, which is applied at those pixels where dual-frequency measurements are available.

7.1 A review of previous dual-frequency algorithms

When dual-frequency measurements are available at n range bins, the number of independent measurements is $2n + 2$, meaning that $2n$ unknown parameters can be estimated without using constraints such as an $R–D_m$ relation. Many retrieval algorithms have been proposed for this problem. In many studies, the ratio of Z_e between the two frequencies, known as the dual-frequency ratio (DFR) is used to retrieve DSD parameters. For example, Meneghini et al. (1997) proposed a retrieval method using DFR and SRT. Mardiana et al. (2004) did not use SRT and instead applied a retrieval method to solve for two DSD parameters from the dual-frequency Z_m values only (MA04). However, MA04 does not perform well with heavy precipitation (Rose and Chandrasekar 2005). Thus, Rose and Chandrasekar (2006a, b) used a constraint on the DSD parameters to obtain a stable solution. Adhikari et al. (2007) tried to improve MA04 by using a differential attenuation between the two frequencies estimated by the profile of Z_m values. Seto and Iguchi (2011) showed that multiple solutions always exist when solving for two DSD parameters from dual-frequency Z_m values at a single range bin and that MA04 becomes less accurate for heavier precipitation or when path lengths through the precipitation are longer. In the pre-launch phase of DPR, Seto et al. (2013) developed an algorithm, which is applicable to both single-frequency and dual-frequency measurements, that combines the Hitschfeld-Bordan and DFR methods known as the HB-DFR method. For the DPR

algorithms (version03B), Seto and Iguchi (2015) added SRT to the HB-DFR method.

In theory, DSD parameters can be estimated using DFR; however, a small error in DFR can result in large errors in D_m and R. Moreover, at lower range bins, attenuation correction for Z_m can cause additional error in DFR. Thus, version 03B of the dual-frequency algorithm was less accurate than the KuPR algorithm in many cases. In version 04 and later versions, DFR has not been used in the dual-frequency algorithm.

7.2 Overview of the dual-frequency algorithm in version 06A

In the dual-frequency algorithm for the DPR, a pixel is judged to be a precipitation pixel if either KuPR or KaPR determines it to be a precipitation pixel. For a precipitation pixel, the DSD and related variables are derived for range bins from the storm top to the surface. If the storm top range bins for KuPR and KaPR differ, then the higher altitude is chosen. Similarly, if the surface range bins for KuPR and KaPR differ, then the higher altitude is chosen.

As described in Section 6.1, range bins are independently classified as rain certain, rain possible, and no rain by KuPR and KaPR. Depending on the combination of range bin types, one of the following is selected to be used for the forward retrieval method in each range bin: (1) Z_m of KuPR, (2) Z_m of KaPR, (3) Z_e of KuPR, or (4) Z_e of KaPR. Table 2 shows the selection for each combination of range bin types, where Z_m is preferable to Z_e and KuPR is preferable to KaPR. If (1) or (2) is selected, the range bin is judged as rain certain in the dual-frequency algorithm, and the forward retrieval method described in Section 6.2a is applied to retrieve the DSD parameters and related variables. If (3) or (4) is selected, the range bin is judged as rain possible in the dual-frequency algorithm, and the forward retrieval method described in Section 6.2b is applied to retrieve the DSD parameters and related variables. In any case, Z_e and k are calculated from the DSD parameters for both KuPR and KaPR, which implies that KuPR can be used at one range bin and KaPR for another along a particular profile. The possibility to selectively use KuPR and KaPR is one of the dual-frequency algorithm's advantages. If both KuPR and KaPR judge a range bin as being a no-rain type, the dual-frequency algorithm judges the range bin as no-rain, meaning that $R = 0$ and $k = 0$. Z_e, N_w, and D_m are then set to missing or indeterminant.

The forward retrieval method is applied for different values of ε from 0.2 to 5.0, after which the results

Table 2. Information used at a range bin in the forward retrieval method in the dual-frequency algorithm depending on the combination of range bin types by KuPR and KaPR. Range bin type in the dual-frequency algorithm is shown in parentheses.

KaPR ⟍ KuPR	Rain certain	Rain possible	No rain
Rain certain	(1) Z_m of KuPR (rain certain)	(1) Z_m of KuPR (rain certain)	(1) Z_m of KuPR (rain certain)
Rain possible	(2) Z_m of KaPR (rain certain)	(3) Z_e of KuPR (rain possible)	(3) Z_e of KuPR (rain possible)
No rain	(2) Z_m of KaPR (rain certain)	(4) Z_e of KaPR (rain possible)	None of (1)–(4) (no rain)

are evaluated to select ε (as explained in Section 7.3). The NUBF parameter is calculated by PIA_{fin} as estimated by single-frequency algorithms. Basically, the PIA_{fin} of the KuPR algorithm is used. If the NUBF parameter cannot be estimated from the KuPR algorithm, the PIA_{fin} of the KaPR algorithm is used. If the NUBF parameter cannot be estimated from the KaPR algorithm, uniformity is assumed.

7.3 Evaluation

The results of the forward retrieval method are evaluated to select the best value of ε from a range between 0.2 and 5.0 using two steps as in the single-frequency algorithms (explained at the beginning of Section 6.3). Using multiple criteria, the scores for F_1–F_5 are determined at each step and the value of ε that minimizes $F = F_1 + F_2 + F_3 + F_4 + F_5$ is selected.

a. Probability distribution of ε

As in the single-frequency algorithms, $x = \log_{10}\varepsilon$ is assumed to follow a normal distribution and the probability density function of x is given in Eq. (95). The DSD database is not used and $\mu_x = 0$ and $\sigma_x = 0.1$.

b. SRT

The difference in PIA values between KuPR and KaPR is denoted by δPIA, where

$$\delta\text{PIA} \equiv \text{PIA}[\text{KaPR}] - \text{PIA}[\text{KuPR}]. \tag{100}$$

The dual-frequency SRT (DSRT) estimate of δPIA can be expressed as

$$
\begin{aligned}
\delta\text{PIA}_{\text{DSRT}} = & \{dB\sigma_e^0[\text{KaPR}] - dB\sigma_m^0[\text{KaPR}]\} \\
& - \{dB\sigma_e^0[\text{KuPR}] - dB\sigma_m^0[\text{KuPR}]\} \\
= & \{dB\sigma_e^0[\text{KaPR}] - dB\sigma_e^0[\text{KuPR}]\} \\
& - \{dB\sigma_m^0[\text{KaPR}] - dB\sigma_m^0[\text{KuPR}]\}.
\end{aligned} \tag{101}
$$

By taking the difference in σ^0 between KaPR and KuPR, variations in σ^0 caused by changes in surface scattering characteristics are mitigated (Meneghini

et al. 2015). From the sampled data, the standard deviation of $\{dB\sigma_e^0[\text{KaPR}] - dB\sigma_e^0[\text{KuPR}]\}$ is calculated to be σ_{DSRT}.

After the forward retrieval method calculates k for all range bins, the PIA_g values are calculated for KuPR and KaPR using Eq. (21). These values are then converted to PIA_{g0} using Eq. (91). δPIA_{g0} is calculated as

$$\delta\text{PIA}_{g0} \equiv \text{PIA}_{g0}[\text{KaPR}] - \text{PIA}_{g0}[\text{KuPR}]. \tag{102}$$

The conditional probability of $\delta\text{PIA}_{\text{DSRT}}$ when δPIA_{g0} is true is

$$
\begin{aligned}
& p_{20}(\delta\text{PIA}_{\text{DSRT}}|\delta\text{PIA}_{g0}) \\
& = \frac{1}{\sqrt{2\pi}\sigma_{\text{DSRT}}}\exp\left[-\frac{(\delta\text{PIA}_{\text{DSRT}} - \delta\text{PIA}_{g0})^2}{2\sigma_{\text{DSRT}}^2}\right].
\end{aligned} \tag{103}
$$

In the maximum likelihood method, the product of p_1 and p_{20} is maximized, which is equivalent to minimizing $F_1 + F_2$,

where

$$F_1 = \frac{(x - \mu_x)^2}{\sigma_x^2}, \tag{104}$$

and

$$F_2 = \frac{(\delta\text{PIA}_{\text{DSRT}} - \delta\text{PIA}_{g0})^2}{\sigma_{\text{DSRT}}^2}. \tag{105}$$

DSRT can be used only when it is reliable (i.e., σ_{DSRT} is smaller than 10 dB) and the SRT values for KuPR and KaPR are not saturated. If DSRT is not used, the single-frequency SRT is used according to the following order of priority: [1] KaPR's SRT (not saturated), [2] KuPR's SRT (not saturated), [3] KaPR's SRT (saturated), [4] KuPR's SRT (saturated), and [5] no SRT. Table 3 shows the selection based on single-frequency SRT conditions. If [1] or [2] is selected, $F_2 = E_2$. If [3] or [4] is selected, $F_2 = E_2$ only if $\text{PIA}_{g0} < \text{PIA}_{\text{SRT}}$. Otherwise, $F_2 = 0$. In the case of [5], $F_2 = 0$. The possibility to selectively use DSRT or one of the single-frequency SRT estimates is one of the dual-frequency algorithm's advantages.

Table 3.   Selection of SRT when DSRT is not used in the dual-frequency algorithm.

KaPR's SRT ⟍ KuPR's SRT	Reliable and not saturated	Saturated	Not reliable
Reliable and not saturated	[1] KaPR's SRT (not saturated)	[2] KuPR's SRT (not saturated)	[2] KuPR's SRT (not saturated)
Saturated	[1] KaPR's SRT (not saturated)	[3] KaPR's SRT (saturated)	[4] KuPR's SRT (saturated)
Not reliable	[1] KaPR's SRT (not saturated)	[3] KaPR's SRT (saturated)	[5] no SRT

c.   ZfKa method

At a range bin classified as rain certain by both KuPR and KaPR, the Z_m of KaPR is not used in the forward retrieval method, but rather is used to evaluate ε. The Z_f of KaPR is calculated from the Z_m of KaPR using Eq. (19) in the uniform case and Eq. (84) in non-uniform cases. This Z_f value is denoted by Z_{f1}. The Z_f of KaPR is calculated from the DSD parameters estimated in the forward retrieval method using Eq. (20) in the uniform case and Eq. (92) in non-uniform cases. This Z_f is denoted by Z_{f2}. Here, f_3 is given as

$$f_3 = \begin{cases} (\mathrm{dB}Z_{f2} - \mathrm{dB}Z_m)^2 & (Z_{f2} < Z_m) \\ 0 & (Z_m \leq Z_{f2} \leq Z_{f1}), \\ (\mathrm{dB}Z_{f2} - \mathrm{dB}Z_{f1})^2 & (Z_{f1} < Z_{f2}) \end{cases}$$

(106)

and F_3 is calculated as the average of f_3 at range bins that are classified as rain certain by both KuPR and KaPR. Using F_3 to evaluate ε is known as the ZfKa method.

The ZfKa method shares some similarity with SRT. In SRT, $\mathrm{dB}\sigma_m^0 + \mathrm{PIA}_{\mathrm{SRT}}$ is expected to be closer to $\mathrm{dB}\sigma_e^0$ according to Eq. (22). In any event, $\mathrm{PIA}_{\mathrm{SRT}}$ should be positive or $\mathrm{dB}\sigma_m^0 + \mathrm{PIA}_{\mathrm{SRT}}$ is required to be larger than $\mathrm{dB}\sigma_m^0$. The ZfKa method uses the precipitation echo rather than the surface echo. $\mathrm{dB}\sigma_m^0$, $\mathrm{dB}\sigma_m^0 + \mathrm{PIA}_{\mathrm{SRT}}$ and $\mathrm{dB}\sigma_e^0$ are replaced by Z_m, Z_{f2}, and Z_{f1}. Z_{f2} is expected to be closer to Z_{f1}, and Z_{f2} must be larger than the Z_m of KaPR. Therefore, f_3 is defined as explained above.

The ZfKa method is not used in the single-frequency algorithms and is one of the dual-frequency algorithm's advantages. If no range bins are classified as rain certain by both KuPR and KaPR, the ZfKa method is not used and $F_3 = 0$.

d.   Optional criteria

Usually, $F = F_1 + F_2 + F_3$ because $F_4 = F_5 = 0$; however, F_4 and F_5 are given as follows in some cases.

In the same way that E_3 is defined in the single-

frequency algorithm, F_4 is the average of the square of ΔZ_f at rain-certain range bins. If D_m has a solution at all rain-certain range bins, then $F_4 = 0$.

In the same way that E_4 is defined in the single-frequency algorithm, F_5 is set equal to the variance of $\mathrm{dB}R$ (dB mm h^{-1}) at range bins in liquid phase if the SRT is saturated or SRT not used ([3], [4], or [5] is selected in Section 7.3b). Otherwise, $F_5 = 0$.

8.   Performance of the DPR algorithms

The outputs of DPR algorithms are stored in the KuPR, KaPR, and dual-frequency Level-2 data products, and Version 06A products for June 2016 were statistically analyzed. The purpose of this analysis is to check algorithm performance, not to validate the outputs with external validation datasets or investigate local or seasonal changes. Many other studies deal with the validation of DPR Level-2 products with regional ground-based precipitation measurements (e.g., Speirs et al. 2017; Petracca et al. 2018; Watters et al. 2018; Ma et al. 2020).

In this section, R represents the precipitation rate at the surface. The KuPR Level-2 product is called KuPR for short. The KaPR Level-2 product consists of normal scan, referred to as KaPR, and interleaved scan, referred to as KaHS, results. Here, the dual-frequency product is referred to as Dual. To compare KuPR and Dual with KaPR and KaHS, only the inner swath pixels are used.

8.1   Overview

Table 4 summarizes the precipitation frequency R_f (i.e., the ratio of the number of precipitation pixels to the number of measurement pixels), the precipitation amount R_{sum} (i.e., the sum of R divided by the number of measurement pixels; in mm per 30 days), the conditional average of ε (i.e., the sum of ε divided by the number of precipitation pixels), and the conditional average of precipitation rate R_{ave} (i.e., the sum of R divided by the number of precipitation pixels; in mm h^{-1}) for KuPR, KaPR, KaHS, and Dual.

The R_f for KaPR is the lowest of the four and is less

Table 4. R_f, R_{sum}, ε, and R_{ave} in KuPR, KaPR, KaHS, and Dual.

	Precipitation frequency R_f	Precipitation Amount R_{sum} [mm (30 days)$^{-1}$]	Average of ε	Average precipitation rate R_{ave} (mm h^{-1})
KuPR	0.06209	67.01	0.868	1.499
KaPR	0.03086	46.98	0.869	2.115
KaHS	0.05468	48.81	0.877	1.240
Dual	0.06242	69.16	0.923	1.539

than half that of KuPR. This is because of differences in sensitivity between the channels. The minimum detectable radar reflectivity factor is 15.46 dBZ for KuPR and 19.18 dBZ for KaPR (Masaki et al. 2021). The R_f for KaHS is lower than that for KuPR, whereas the minimum detectable radar reflectivity factor of KaHS (13.71 dBZ) is better than that of KuPR. This is because of pixel-level differences in precipitation judgment. The requirements for a precipitation pixel are more strict for KaHS than KuPR because KaHS has a lower vertical resolution. Figure 11 shows a histogram of R for KuPR, KaPR, KaHS, and Dual. The vertical axis shows frequency, which is defined as the ratio of the number of pixels at each 1 dBR bin to the total number of pixels. Some precipitation pixels have precipitation aloft but none at the surface, and these pixels are not included in this figure. The lower limit of R is approximately 0.1 mm h^{-1} for KuPR and KaHS; however, it is slightly better for KaHS because KaHS has higher sensitivity than KuPR. The lower limit for KaPR is approximately 0.3 mm h^{-1}. KaPR misses many precipitation pixels; however, these are mostly light precipitation pixels. Hence, the R_{sum} for KaPR is not very different from that of KaHS as shown in Table 4. KuPR and Dual have nearly the same R_f, but have different ε and R_{ave}. The differences among these products are investigated further below.

Figure 12 shows R_f and R_{sum} for each angle bin. The horizontal axis shows the angle bin number where 12 (12.5) has been added to angle bin number for KaPR (KaHS). The R_f of KuPR and Dual are almost identical. Generally, R_f and R_{sum} are higher at smaller incidence angles (i.e., when the angle bin number is closer to 25). The R_f of KuPR and Dual show depressions around angle bin numbers 19 and 32, whereas R_{sum} does not. Kubota et al. (2016) showed under-corrections or over-corrections at off-nadir angles due to a technique for reducing sidelobe clutter. This can affect R_f in off-nadir angle bins. Therefore, it is thought that this technique deleted some light precipitation echoes there, and improvements of the technique remain a task for future work.
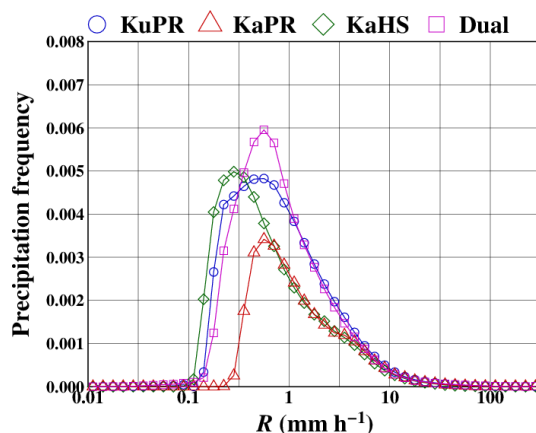
Fig. 11.   Histogram of R.

8.2   Classification by precipitation judgments

If precipitation is detected at a pixel by either KuPR or KaPR, Dual judges it as a precipitation pixel. If precipitation is not detected by KuPR but is detected by KaPR, the pixel is classified as type-1. The R_f in Dual is slightly higher than in KuPR due to type-1 classifications. If precipitation is not detected by KaPR but is detected by KuPR, the pixel is classified as type-2. Lastly, if precipitation is detected by both KuPR and KaPR, the pixel is classified as type-3. Table 5 shows R_f, R_{sum}, ε, and R_{ave} values for each type (i.e., type-1, type-2, and type-3) in Dual. Type-1 has a very small R_f. Type-2 and type-3 have nearly identical R_f; however, type-3 shows a much higher R_{sum} than type-2. Type-1 and type-2 have smaller R_{ave} values as they are mainly for light precipitation.

Table 5 also shows R_{sum}, ε, and R_{ave} in KuPR and KaPR for each type; however, KuPR has no type-1 precipitation pixels and KaPR has no type-2 precipitation pixels. For type-1 pixels, KaPR has smaller ε, but higher R_{ave} values than Dual. Additionally, KaPR's Z_m may be overestimated for type-1. For type-2 pixels, Dual has higher ε and R_{ave} than KuPR.

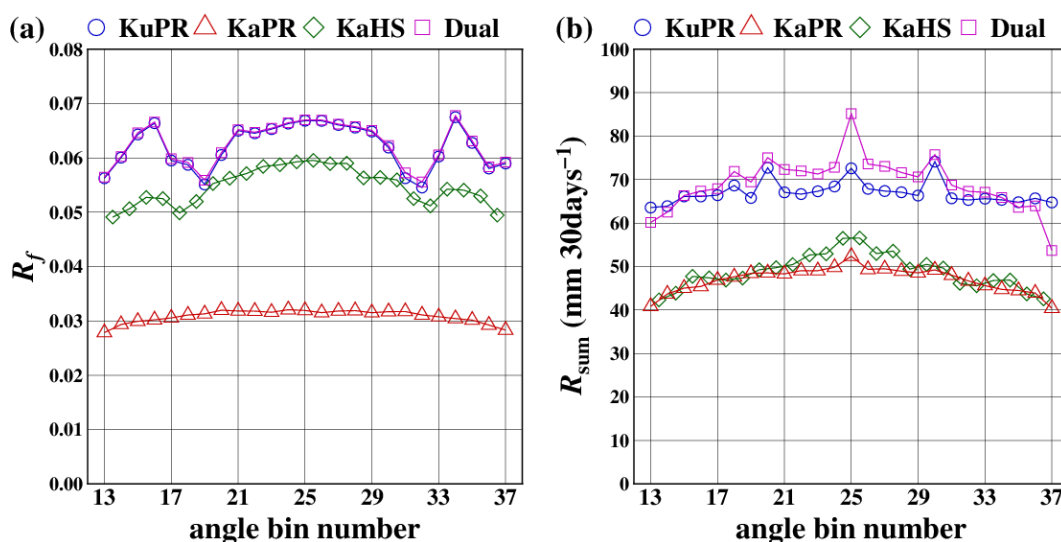For type-3 pixels, KuPR, KaPR, and Dual have es-

Fig. 12. Angle bin dependence of (a) R_f and (b) R_{sum}.

Table 5. R_f, R_{sum}, ε, and R_{ave} for types 1–3 in KuPR, KaPR, and Dual. R_{sum} has a unit of mm 30 days^{-1} and R_{ave} has a unit of mm h^{-1}.

	Dual				KuPR			KaPR		
	R_f	R_{sum}	ε	R_{ave}	R_{sum}	ε	R_{ave}	R_{sum}	ε	R_{ave}
Type1	0.00033	0.09	0.878	0.359				0.20	0.847	0.844
Type2	0.03157	9.78	0.959	0.430	9.08	0.869	0.400			
Type3	0.03052	59.30	0.885	2.698	57.93	0.867	2.636	46.78	0.870	2.128
All	0.06242	69.16	0.923	1.539	67.01	0.868	1.499	46.98	0.869	2.115

timates and they are compared. KuPR and KaPR have similar ε, but KuPR has higher R_{ave}. Dual has slightly higher ε and R_{ave} than KuPR. Figure 13 shows ε and R_{ave} for each angle bin. The ε value of Dual shows a tendency to be higher at smaller incidence angles (i.e., incidence angle dependence), whereas KuPR and KaPR do not show incidence angle dependence. The R_{ave} values in Dual and KaPR show incidence angle dependence but KuPR values do not. In Dual, ε and R_{ave} both show a large discontinuity between angle bins 36 and 37 because of a programming error at angle bin 37. This error will be corrected in the next version of the DPR algorithms.

8.3 Dual-frequency methods

Although Dual basically uses KuPR's Z_m in the forward retrieval method like KuPR, it uses the ZfKa method and DSRT (called dual-frequency methods) to determine ε. Table 6 shows R_f, R_{sum}, ε, and R_{ave} with and without the use of the ZfKa method and DSRT in Dual. For R_f and R_{sum}, the ratio to those at all precipitation pixels is shown as well. The ZfKa method is used for approximately 80 % of pixels in R_f and for approximately 95 % of R_{sum}. DSRT is used for about 80 % of pixels in R_f and for around 85 % of R_{sum}. No dual-frequency methods are used for 7.27 % of pixels in R_f and 1.45 % of R_{sum}.

Dual-frequency methods are used not only for type-3 pixels, but also for type-1 and type-2 pixels. In a type-1 (type-2) pixel judged to be a no-precipitation pixel by the KuPR (KaPR) algorithm the ZfKa method is used if a range bin is judged to be rain certain by both the KuPR and KaPR radars in the dual-frequency algorithm. This can happen when the number of range bins where precipitation is detected is lower than some threshold value. In such cases, the pixel is judged to be a no-precipitation pixel in the single-frequency algorithm. Because σ^0 is always measured by both the KuPR and KaPR radars, DSRT may be used at type-1 and type-2 pixels in the dual-frequency algorithm.
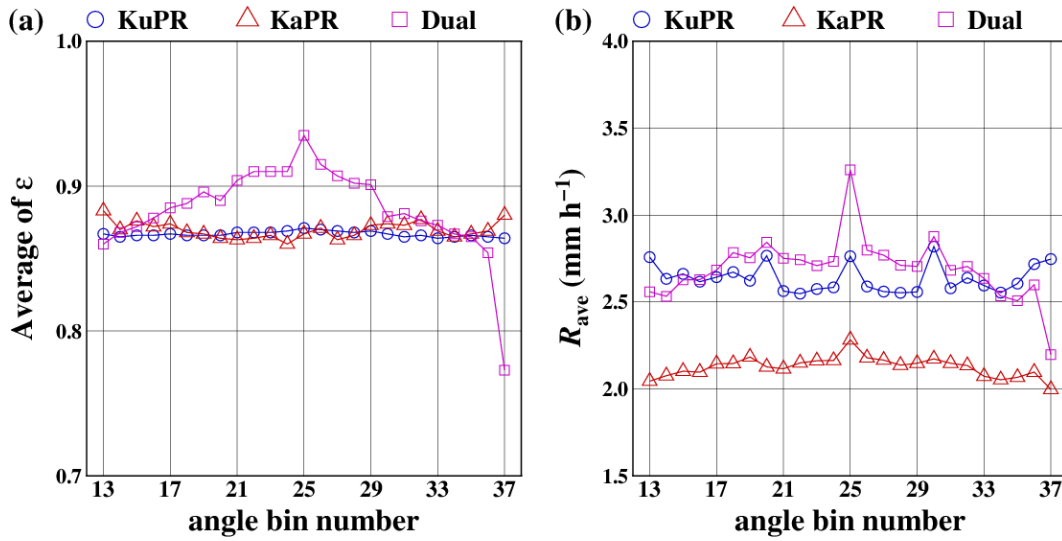
Fig. 13.   Angle bin dependence of (a) ε and (b) R_{ave} for type-3 pixels.

Table 6. R_f, R_{sum}, ε, and R_{ave} with and without the use of the ZfKa method and DSRT in Dual, where (ratio) is the ratio of R_f and R_{sum} to all precipitation pixels.

ZfKa is used?	DSRT is used?	R_f	(ratio)	R_{sum} [mm (30 days)$^{-1}$]	(ratio)	ε	R_{ave} (mm h^{-1})
Yes	Yes	0.04178	(66.93 %)	57.28	(82.82 %)	0.897	1.904
Yes	No	0.00788	(12.62 %)	8.67	(12.54 %)	0.935	1.529
No	Yes	0.00823	(13.18 %)	2.21	(3.19 %)	0.997	0.373
No	No	0.00454	(7.27 %)	1.00	(1.45 %)	0.998	0.307

Table 6 shows that ε is nearly 1 when the ZfKa method is not used. This implies that the ZfKa method affects ε severely and may cause the incidence angle dependence shown in Fig. 13a. Figure 13 can be drawn separately for cases with and without the use of the ZfKa method; however, the number of samples differs notably between the cases and R_{ave} is as well. Therefore, test products were prepared to check whether the ZfKa method or other factors affect ε and its incidence angle dependence. Table 7 lists the settings of the test products. The angle bin dependence of ε and R_{ave} for type-3 pixels for the standard product and test products in Dual are shown in Fig. 14.

Test product 1 does not use the ZfKa method and has higher ε and R_{ave} than the standard product. Additionally, the incidence angle dependence of ε is clearly seen in test product 1. This means that the ZfKa method affects ε, but it is not a unique cause of incidence angle dependence of ε.

Test products 2 and 4 do not use DSRT but rather use single-frequency SRTs. Test product 2 prefers KaPR's SRT to KuPR's SRT, whereas test product 4 prefers KuPR's SRT to KaPR's SRT. Both products use the ZfKa method. Test product 2 (4) shows lower (higher) ε and R_{ave} than the standard product. This reflects the bias in PIA$_{SRT}$ as well as the reliability of SRT. KuPR's SRT is not very reliable, thus ε is not largely modified from 1 in test product 4. Both products show incidence angle dependence for ε and R_{ave}.

Test products 3 and 5 use neither the ZfKa method nor DSRT, whereas test product 3 (5) prefers KaPR's (KuPR's) SRT. Because test product 5 is similar to KuPR's standard product except for an a-priori pdf of ε (DSD database is not used in Dual), it shows ε of nearly 1 and no incidence angle dependence in ε or R_{ave}. In contrast, test product 3 shows incident angle dependence of ε and R_{ave}. This implies that the use of KaPR measurements (ZfKa method, DSRT, or KaPR's SRT) causes the incidence angle dependence of ε and R_{ave}. This problem should be investigated further to improve DPR algorithms in the next version.

Table 7.   Settings of the test products.

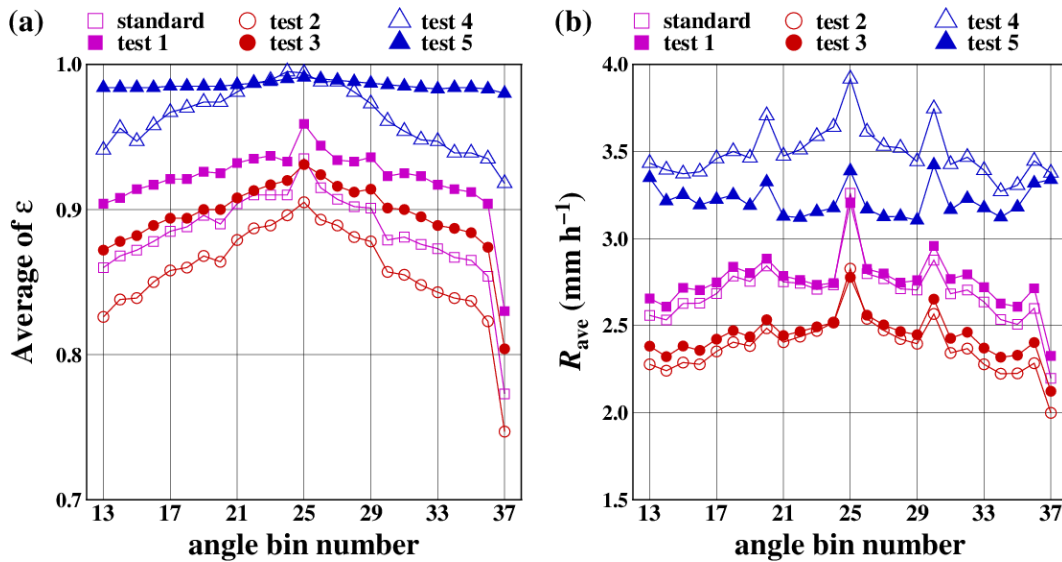| Product number	ZfKa method	DSRT
Standard product	Used	Used
Test product 1	Not used	Used
Test product 2	Used	Not used (KaPR's SRT is preferred)
Test product 3	Not used	Not used (KaPR's SRT is preferred)
Test product 4	Used	Not used (KuPR's SRT is preferred)
Test product 5	Not used	Not used (KuPR's SRT is preferred)

Fig. 14.   Angle bin dependence of (a) ε and (b) R_{ave} for type-3 pixels in Dual with different options for the use of dual-frequency methods.

8.4   Selective use of precipitation and surface echoes in Dual

Dual can use KuPR and KaPR precipitation and surface echoes. For type-3 pixels, comparisons among the KuPR, KaPR, and Dual estimates show the characteristics of each product as well as the advantages of Dual.

a.   Precipitation echo at CFB

The range bin type at CFB is analyzed. Table 8 shows the ratio of the number of rain certain, rain possible, and no rain pixels at CFB to the number of type-3 pixels. In KuPR, the ratio of rain certain is higher than 90 % and the ratio of rain possible is as high as 5 %. In KaPR, the ratio of rain certain is lower and the ratio of rain possible is higher than in KuPR. In Dual, the ratio of rain certain is higher and the ratio of rain possible is lower than in KuPR.

Figure 15 shows the ratio of the number of pixels

Table 8.   The ratio of the number of pixels with rain certain, rain possible, or no rain at CFB to the number of type-3 pixels.

	KuPR	KaPR	Dual
rain certain at CFB	93.32 %	77.85 %	94.75 %
rain possible at CFB	5.00 %	14.26 %	3.58 %
no rain at CFB	1.68 %	7.89 %	1.66 %

with rain possible at CFB to the number of type-3 pixels, where the horizontal axis is R of KuPR (denoted by R_{Ku}). For a 1 dBR (dB mm h^{-1}) bin of R_{Ku}, the ratio is calculated in KuPR, KaPR, and Dual. Because KuPR is stable, R_{Ku} is used as a scale of precipitation intensity. By taking the common scale as the horizontal axis, it becomes easy to compare the three products. R_{Ku} values below 0.1 mm h^{-1} are not shown as the number of samples is very few (as shown in Fig. 11).
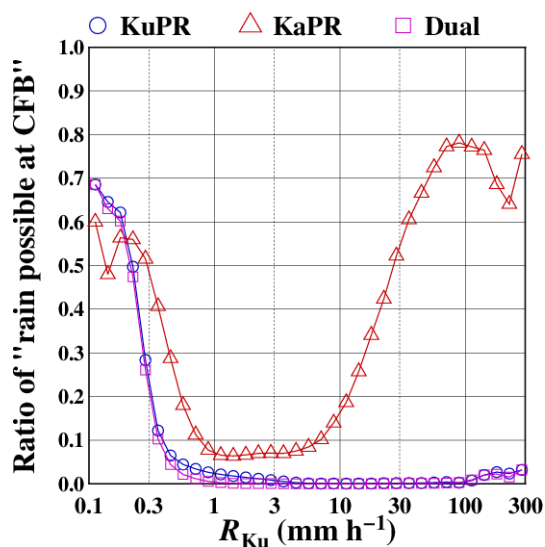
Fig. 15.   The ratio of the number of pixels with rain possible at CFB to the number of type-3 pixels for a 1 dBR bin of R_{Ku}.
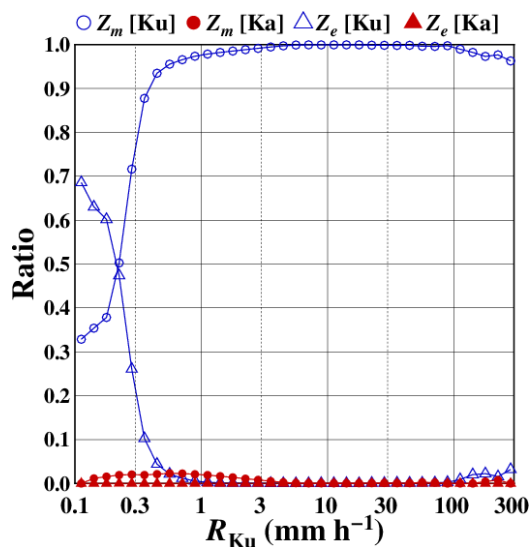

Fig. 16.   The selection of precipitation echo at CFB for type-3 pixels in Dual. The vertical axis shows the ratio of the number of pixels where each of KuPR's D_m, KaPR's D_m, KuPR's Z_e, or KaPR's Z_e is selected to the number of type-3 pixels for a 1 dBR bin of R_{Ku}.

In KuPR, the ratio is high for light precipitation (R_{Ku} < 1 mm h^{-1}). For heavier precipitation, the ratio is smaller except for very heavy precipitation (R_{Ku} > 100 mm h^{-1}). Under very heavy precipitation, a precipitation echo at CFB is missing because of attenuation. In KaPR, the ratio is higher than KuPR for R_{Ku} > 0.3 mm h^{-1}. For light precipitation, this is because the sensitivity of KaPR is lower than that of KuPR. For heavy precipitation (R_{Ku} > 10 mm h^{-1}), it is because attenuation is stronger in KaPR than in KuPR. In Dual, the ratio is almost the same as KuPR but slightly lower than KuPR for light precipitation (0.3 mm h^{-1} < R_{Ku} < 1 mm h^{-1}).

Figure 16 shows the precipitation echo selection at CFB in Dual. The horizontal axis is the same as that in Fig. 15. As explained in Section 7.2, the order of priority is (1) KuPR's Z_m, (2) KaPR's Z_m, (3) KuPR's Z_e, and (4) KaPR's Z_e. The vertical axis in Fig. 16 shows the ratio of the number of pixels where each of (1)−(4) is selected at CFB in Dual to the number of type-3 pixels for a 1 dBR bin of R_{Ku}. For very light precipitation (R_{Ku} ~ 0.1 mm h^{-1}), (3) is mainly used. For heavier precipitation, the ratio of (1) increases and that of (3) decreases. When 3 mm h^{-1} < R_{Ku} < 100 mm h^{-1}, (1) is almost always used. For very heavy precipitation (R_{Ku} > 100 mm h^{-1}), (3) is sometimes used. (2) is used for some light precipitation (R_{Ku} ~ 1 mm h^{-1}) and (4) is rarely used.

Figure 17 shows the ratio of the number of pixels

with no rain at CFB in KaPR to the number of type-3 pixels for a 1 dBR bin of R_{Ku}. The ratio is high for light precipitation (R_{Ku} < 3 mm h^{-1}) and almost zero for medium to heavy precipitation (3 mm h^{-1} < R_{Ku} < 100 mm h^{-1}); however, it is several percent for very heavy precipitation (R_{Ku} > 100 mm h^{-1}). The latter is a serious problem as KaPR misses very heavy precipitation. When R_{Ku} > 100 mm h^{-1}, the CFB range bin is judged as rain possible for approximately 70 % of cases (in Fig. 15) but judged as no rain for several percent (in Fig. 17). The classification criteria explained in Section 6.1, i.e., "If eight or more rain-certain range bins in the liquid phase exist above the range bin, the range bin is judged as rain possible", works well. This rule implies that in most heavy precipitation cases, KaPR will assume rain possible at the CFB.

b.   SRT

As described in Sections 6.3b and 7.3b, SRT is not used in some cases and saturated in others. If SRT is used and is not saturated, it is referred to as "SRT is normally used". Table 9 shows the ratio of the number of "SRT is normally used", "SRT is saturated", and "SRT is not used" pixels to the number of type-3 pixels. In KuPR, SRT is normally used for more than 90 % of type-3 pixels and SRT is not used for the rest.
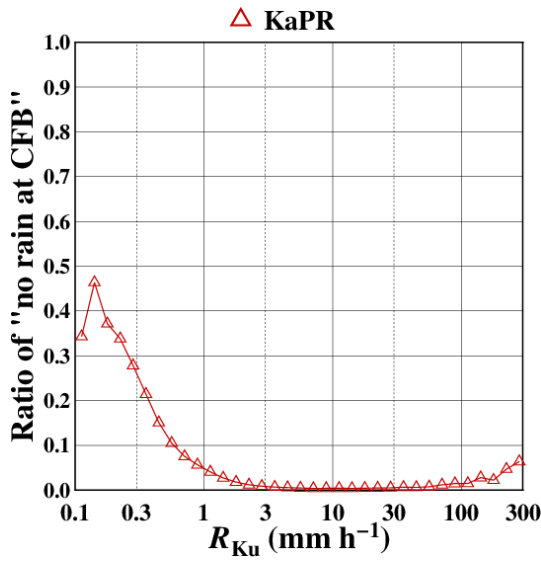
Fig. 17.   The ratio of the number of pixels with no rain at CFB to the number of type-3 pixels in KaPR for a 1 dBR bin of R_{Ku}.

Table 9.   The ratio of the number of pixels where SRT is normally used, SRT is saturated, and SRT is not used to the number of type-3 pixels.

	KuPR	KaPR	Dual
SRT is normally used	91.57 %	98.13 %	99.32 %
SRT is saturated	0.00 %	0.49 %	0.00 %
SRT is not used	8.43 %	1.38 %	0.67 %

KaPR and the ratio of SRT is saturated is almost zero. The ratio of SRT is not used is lower than in KuPR and in KaPR.

Figure 18a shows the ratio of the number of pixels where SRT is not used to the number of type-3 pixels for a 1 dBR bin of R_{Ku}. In KuPR, SRT is not used for light precipitation ($R_{Ku} < 3$ mm h^{-1}) or for very heavy precipitation ($R_{Ku} > 100$ mm h^{-1}). In KaPR, the ratio is lower for light precipitation ($R_{Ku} < 3$ mm h^{-1}) but higher for heavy precipitation ($R_{Ku} > 30$ mm h^{-1}). For light precipitation, PIA is smaller and SRT is less reliable for KuPR than for KaPR. For heavy precipitation, PIA$_{SRT}$ is sometimes much higher than PIA$_{HB}$, in which case SRT is not used. This is not only an error for PIA$_{SRT}$, but PIA$_{HB}$ also tends to be underestimated for heavy precipitation, particularly in KaPR. This should be improved in the next version. In Dual, the ratio of SRT is not used is lower than in KuPR and KaPR for both light and heavy precipitation.

Figure 18b shows the ratio of the number of pixels

The ratio of "SRT is saturated" for KuPR is almost zero. For KaPR, the SRT is normally used for more than 98 % of type-3 pixels. The ratio of SRT is not used is lower than for KuPR, but the ratio of SRT is saturated is not zero (0.49 %). In Dual, the ratio of SRT is normally used is higher than in KuPR and in
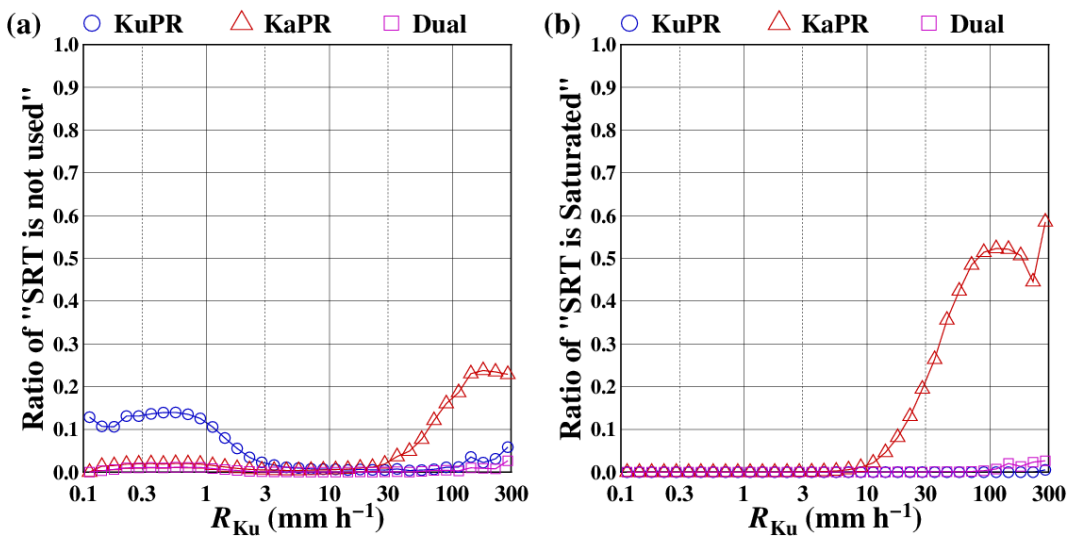

Fig. 18.   The ratio of the number of pixels where (a) SRT is not used and (b) SRT is saturated to the number of type-3 pixels for a 1 dBR bin of R_{Ku}.
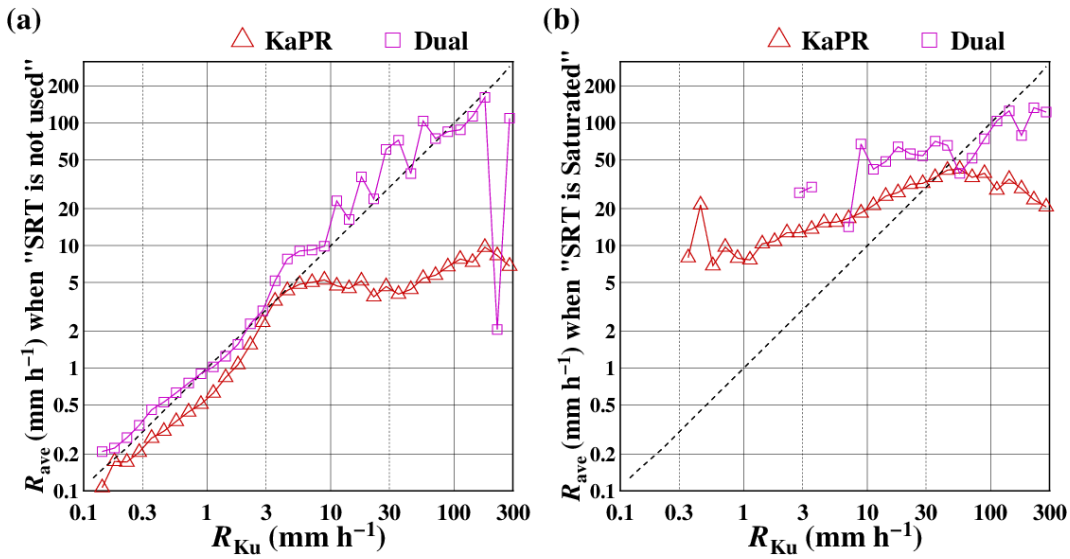
(a)

(b)

Fig. 19. R_{ave} of type-3 pixels in KaPR and Dual when (a) SRT is not used and (b) SRT is saturated for a 1 dBR bin of R_{Ku}.

where SRT is saturated to the number of type-3 pixels. In KaPR, the ratio is high when $R_{Ku} > 10$ mm h^{-1}. In Dual, SRT is saturated is found only for very heavy precipitation ($R_{Ku} > 100$ mm h^{-1}).

Figure 19 shows R_{ave} for KaPR and Dual along the vertical axis, whereas the horizontal axis is R_{Ku}. In cases where SRT is not used, the R_{ave} for KaPR has a ceiling around 10 mm h^{-1} so that severe underestimation happens. In cases where SRT is saturated, R_{ave} for KaPR is not very accurate; however, it is much higher than in the previous case. This suggests that it is better to use SRT even if it is saturated. When $R > 100$ mm h^{-1}, SRT is saturated for about 50 % of the pixels and SRT is not used for about 25 % (Fig. 18). The cases where SRT is not used should be avoided as much as possible.

Figure 20 shows the selection of SRT in Dual. As explained in Section 7.2, the order of priority is DSRT, KaPR's SRT, KuPR's SRT, KaPR's SRT (saturated), and KuPR's SRT (saturated). DSRT is mostly selected when 3 mm h^{-1} < R_{Ku} < 10 mm h^{-1}. The vertical axis in Fig. 20 shows the ratio of the number of pixels where DSRT, KaPR's SRT, or KuPR's SRT is selected in Dual to the number of type-3 pixels for a 1 dBR bin of R_{Ku}. For light precipitation ($R_{Ku} < 3$ mm h^{-1}), KaPR's SRT is selected for approximately 10 % of the cases. For heavy precipitation ($R_{Ku} > 10$ mm h^{-1}), KuPR's SRT becomes dominant. By selecting different SRTs, SRT is not used is mostly avoided in Dual.
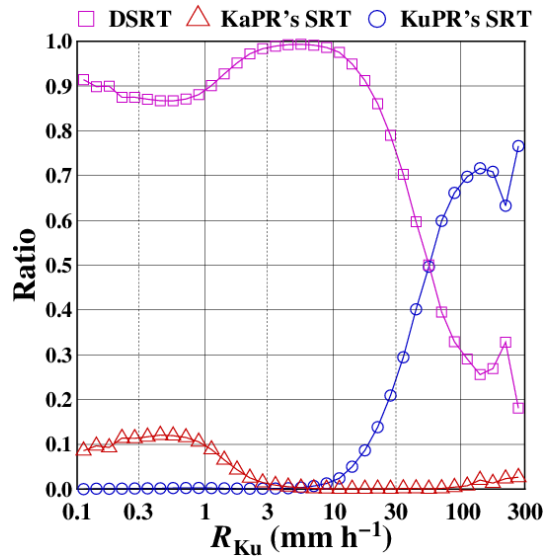

Fig. 20.   The selection of SRT for type-3 in Dual. The vertical axis shows the ratio of the number of pixels where DSRT, KaPR's SRT, or KuPR's SRT is selected to the number of type-3 pixels for a 1 dBR bin of R_{Ku}.

Table 10.   Characteristics of the DPR algorithms and previous algorithms.

Algorithm Version	Single-frequency algorithm		Dual-frequency algorithm		
	PR Version 7	DPR Version 06A	(Seto et al. 2013)	DPR Version 03B	DPR Version 06A
DSD constraint	k–Z_e relation	R–D_m relation	k–Z_e relation	k–Z_e relation	R–D_m relation
DSD database	Not used	Used	Not used	Not used	Not used
DFR method	Not used	Not used	Used	Used	Not used
ZfKa method	Not used	Not used	Not used	Not used	Used
SRT	Used	Used	Not used	Used (DSRT)	Used (DSRT)
NUBF correction	Used (ε constant)	Used (D_m constant)	Not used	Not used	Used (D_m constant)

9.   Summary

9.1   Characteristics of the precipitation rate retrieval algorithm

The precipitation rate retrieval algorithms for the DPR algorithms (version 06A) are developed. Major changes from version 03B (Seto and Iguchi 2015) include the introduction of the R–D_m relation (instead of the k–Z_e relation), NUBF correction, DSD database (single-frequency algorithms only), and the ZfKa method (instead of the DFR method; dual-frequency algorithm only). Table 10 summarizes the characteristics of the updated DPR algorithms (version 06A) in comparison to version 03B and other previous algorithms.

For the KuPR algorithm, a method like that of the PR algorithm is used, but with an R–D_m relation instead of a k–Z_e relation. The R–D_m relation is used also for the KaPR algorithm and the dual-frequency algorithm, meaning that the three algorithms share a common constraint on the DSD.

The dual-frequency algorithm has the same structure as the single-frequency algorithms; the forward retrieval method is applied to Z_m or Z_e at a single-frequency with an assumed ε and the results are then evaluated to select the best ε. The DFR is not used because it does not always work well under real measurement conditions. The dual-frequency algorithm has the advantages that it can select KuPR or KaPR for the precipitation echoes and use additional evaluation criteria such as the ZfKa method and DSRT. When DSRT is not available, KaPR's SRT or KuPR's SRT can be selected. The dual-frequency algorithm has more evaluation criteria to select ε, whereas the single-frequency algorithm mainly uses a single-frequency SRT, which is not very accurate, particularly for light precipitation. The DSD database has been introduced to convert information obtained from the dual-frequency algorithm for application to the single-frequency algorithms.

The NUBF correction used in the DPR algorithms assumes that N_w varies horizontally, that D_m is constant in a beam, and that the R–D_m relation holds for the average values. These assumptions differ from those used in the PR algorithm, where k varies horizontally in a beam and the k–Z_e relation holds in any sub-beam.

9.2   Performance of the precipitation rate retrieval algorithm

From the statistical analysis of outputs, the following results are found.

In the KuPR algorithm, ε and R do not show significant incidence angle dependence, whereas R shows incidence angle dependence in the KaPR algorithm and ε and R show incidence angle dependence in the dual-frequency algorithm. No major problems have been found in the KuPR algorithm.

The KaPR algorithm misses precipitation and surface echoes under heavy precipitation. When the precipitation echo is missing at CFB, the KaPR algorithm usually judges a pixel as rain possible and extrapolates Z_e to estimate the precipitation; it rarely judges the situation as no rain. Even if the surface echo is missing, the saturated SRT is used. However, sometimes SRT is not used for heavy precipitation and severe underestimation occurs.

The dual-frequency algorithm has a higher precipitation frequency than either of the single-frequency algorithms. This follows from the fact that the dual-frequency algorithm assumes the presence of precipitation if either KuPR or KaPR detect precipitation. The precipitation pixels of the dual-frequency algorithm are classified into three types: type-1 (KaPR detects precipitation, but KuPR does not), type-2 (KuPR detects precipitation, but KaPR does not), and type-3 (both KuPR and KaPR detect precipitation). Type-1 is rare, but type-2 and type-3 are found in

Table A1.   Definition of qualitySLV.

Bit(s)	Contents	Value = 0	Value = 1	Value = 2	Value = 3
1	Precipitation pixel?	No	Yes		
2 & 3	SRT	Not used	KuPR' SRT	KaPR's SRT	DSRT
4	SRT is saturated?	No	Yes		
5 & 6	ε	Normal	Lower limit	Upper limit	Error
7	ZfKa method	Not used	Used		
8	Variance of dBR	Not used	Used		
10	NUBF correction	Not used	Used		
14 & 15	NUBF parameter	Normal	Lower limit	Upper limit	Error
18 & 19	Extrapolation of Z_e at or above CFB?	(No-rain)	Yes	No	
20 & 21	Precipitation echoes at and above CFB	(No-rain)	Only KuPR is used	Only KaPR is used	Both KuPR and KaPR are used
22	D_m takes lower limit at or above CFB?	No	Yes		
23	D_m takes upper limit at or above CFB?	No	Yes		
25 & 26	Judgement at CFB	No rain	Rain possible	Rain certain	
27 & 28	Precipitation echo at CFB	Not used	KuPR used	KaPR used	
29 & 30	D_m at CFB	Normal	Lower limit	Upper limit	Error
32	Data quality	Normal	Error		

nearly half of the precipitation pixels.

The dual-frequency algorithm generally uses DSRT; however, it uses KaPR's SRT for light precipitation and KuPR's SRT for heavy precipitation. Cases where the SRT is not used in the dual-frequency algorithm are rare.

The dual-frequency algorithm uses the ZfKa method and DSRT to select the best value of ε not only for type-3 pixels, but for type-1 and type-2 pixels as well. For more than 90 % of the precipitation pixels, either the ZfKa method or DSRT is used.

In the dual-frequency algorithm, ε shows incidence angle dependence. The reason for this has not been clearly shown, but it may be related to the use of KaPR measurements. The improvement of the use of KaPR measurements is important for the next version of the DPR algorithms, which will be applied to measurements after the scan pattern change of KaPR, when all pixels are measured by both radars.

Acknowledgments

Appendix

For the analysis of Level-2 products in Section 8, the variable qualitySLV, a 4-byte integer given at each pixel, is used. Information about the Solver module is contained at bits $1-32$ as shown in Table A1. Some bits with no significant information are omitted from the table. For example, the information about the ZfKa method is at bit 7. qualitySLV is divided by 2^{7-1} and the quotient is divided by 2. If the remainder is 0, the ZfKa method is not used, but if the remainder is 1, it is used. To check judgment at CFB (bits 25 and 26), divide qualitySLV by 2^{25-1} and divide the resulting quotient by 4. At no-precipitation pixels, qualitySLV is generally 0.

References

Adhikari, N. B., T. Iguchi, S. Seto, and N. Takahashi, 2007: Rain retrieval performance of a dual-frequency Precipitation Radar technique with differential-attenuation constraint. *IEEE Trans. Geosci. Remote Sens.*, **45**, 2612–2618.

Atlas, D., and C. W. Ulbrich, 1977: Path- and area-integrated rainfall measurement by microwave attenuation in the 1–3 cm band. *J. Appl. Meteor.*, **16**, 1322–1331.

Awaka, J., M. Le, V. Chandrasekar, N. Yoshida, T. Higashi-uwatoko, T. Kubota, and T. Iguchi, 2016: Rain type classification algorithm module for GPM Dual-frequency Precipitation Radar. *J. Atmos. Oceanic Technol.*, **33**, 1887–1898.

Awaka, J., M. Le, S. Brodzik, T. Kubota, T. Masaki, V.

Chandrasekar, and T. Iguchi, 2020: Improvements of rain type classification algorithms for a full scan mode of GPM Dual-frequency Precipitation Radar. *J. Meteor. Soc. Japan*, in revision

Hitschfeld, W., and J. Bordan, 1954: Errors inherent in the radar measurement of rainfall at attenuating wavelengths. *J. Meteor.*, **11**, 58–67.

Hou, A. Y., R. K. Kakar, S. Neeck, A. A. Azarbarzin, C. D. Kummerow, M. Kojima, R. Oki, K. Nakamura, and T. Iguchi, 2014: The Global Precipitation Measurement mission. *Bull. Amer. Meteor. Soc.*, **95**, 701–722.

Iguchi, T., 2020: Dual-frequency Precipitation Radar (DPR) on the Global Precipitation Measurement (GPM) mission's core observatory. *Satellite Precipitation Measurement. Vol. 1*. Levizzani, V., C. Kidd, D. B. Kirschbaum, C. D. Kummerow, K. Nakamura, and F. J. Turk (eds.), Advances in Global Change Research book series, Springer, 183–192.

Iguchi, T., and R. Meneghini, 2016a: *GPM DPR Ka precipitation profile 2A 1.5 hours 5 km V06 (GPM_2AKa)*. Goddard Earth Sciences Data and Information Services Center, doi:10.5067/GPM/DPR/Ka/2A/06.

Iguchi, T., and R. Meneghini, 2016b: *GPM DPR Ku precipitation profile 2A 1.5 hours 5 km V06 (GPM_2AKu)*. Goddard Earth Sciences Data and Information Services Center, doi:10.5067/GPM/DPR/Ku/2A/06.

Iguchi, T., and R. Meneghini, 2017: *GPM DPR precipitation profile L2A 1.5 hours 5 km V06 (GPM_2ADPR)*. Goddard Earth Sciences Data and Information Services Center, doi:10.5067/GPM/DPR/GPM/2A/06.

Iguchi, T., T. Kozu, R. Meneghini, J. Awaka, and K. Okamoto, 2000: Rain-profiling algorithm for the TRMM precipitation radar. *J. Appl. Meteor.*, **39**, 2038–2052.

Iguchi, T., T. Kozu, J. Kwiatkowski, R. Meneghini, J. Awaka, and K. Okamoto, 2009: Uncertainties in the rain profiling algorithm for the TRMM precipitation radar. *J. Meteor. Soc. Japan*, **87A**, 1–30.

Iguchi, T., S. Seto, R. Meneghini, N. Yoshida, J. Awaka, M. Le, V. Chandrasekar, S. Brodzik, and T. Kubota, 2018: *GPM/DPR level-2 algorithm theoretical basis document*. 127 pp. [Available at https://www.eorc.jaxa.jp/GPM/doc/algorithm/ATBD_DPR_201811_with_Appendix3b.pdf.]

Kojima, M., T. Miura, K. Furukawa, Y. Hyakusoku, T. Ishikiri, H. Kai, T. Iguchi, H. Hanado, and K. Nakagawa, 2012: Dual-frequency Precipitation Radar (DPR) development on the Global Precipitation Measurement (GPM) core observatory. *Proc. SPIE, Earth Observing Missions and Sensors: Development, Implementation, and Characterization II*, **85281A**, doi:10.1117/12.976823.

Kozu, T., T. Kawanishi, H. Kuroiwa, M. Kojima, K. Oikawa, H. Kumagai, K. Okamoto, M. Okumura, H. Nakatsuka, and K. Nishikawa, 2001: Development of precipitation radar onboard the Tropical Rainfall Measuring Mission (TRMM) satellite. *IEEE Trans. Geosci. Remote Sens.*, **39**, 102–116.

Kozu, T., T. Iguchi, T. Kubota, N. Yoshida, S. Seto, J. Kwiatkowski, and Y. N. Takayabu, 2009a: Feasibility of raindrop size distribution parameter estimation with TRMM Precipitation Radar. *J. Meteor. Soc. Japan*, **87A**, 53–66.

Kozu, T., T. Iguchi, T. Shimomai, and N. Kashiwagi, 2009b: Raindrop size distribution modeling from a statistical rain parameter relation and its application to the TRMM precipitation radar rain retrieval algorithm. *J. Appl. Meteor. Climatol.*, **48**, 716–724.

Kubota, T., N. Yoshida, S. Urita, T. Iguchi, S. Seto, R. Meneghini, J. Awaka, H. Hanado, S. Kida, and R. Oki, 2014: Evaluation of precipitation estimates by at-launch codes of GPM/DPR algorithms using synthetic data from TRMM/PR observations. *IEEE J. Sel. Top. Appl. Earth Obs. Remote Sens.*, **7**, 3931–3944.

Kubota, T., T. Iguchi, M. Kojima, L. Liao, T. Masaki, H. Hanado, R. Meneghini, and R. Oki, 2016: A statistical method for the reducing sidelobe clutter for the Ku-band precipitation radar on board the GPM core observatory. *J. Atmos. Oceanic Technol.*, **33**, 1413–1428.

Kubota, T., T. Iguchi, T. Masaki, N. Yoshida, and R. Oki, 2018: Development of a statistical method for reducing sidelobe clutter in high sensitivity mode of GPM/KaPR. *IGARSS 2018 - 2018 International Geoscience and Remote Sensing Symposium*, Valencia, 2018, 8347–8348.

Kubota, T., S. Seto, M. Satoh, T. Nasuno, T. Iguchi, T. Masaki, J. M. Kwiatkowski, and R. Oki, 2020: Cloud assumption of precipitation retrieval algorithms for the Dual-frequency Precipitation Radar. *J. Atmos. Oceanic Technol.*, **37**, 2015–2031.

Kummerow, C., W. Barnes, T. Kozu, J. Shiue, and J. Simpson, 1998: The Tropical Rainfall Measuring Mission (TRMM) sensor package. *J. Atmos. Oceanic Technol.*, **15**, 809–817.

Kuo, K.-S., W. S. Olson, B. T. Johnson, M. Grecu, L. Tian, T. L. Clune, B. H. van Aartsen, A. J. Heymsfield, L. Liao, and R. Meneghini, 2016: The microwave radiometer properties of falling snow derived from nonspherical ice particle models. Part I: An extensive database of simulated pristine crystals and aggregate particles, and their scattering properties. *J. Appl. Meteor. Climatol.*, **55**, 691–708.

Le, M., V. Chandrasekar, and S. Biswas, 2016: Evaluation and validation of GPM dual-frequency classification module after launch. *J. Atmos. Oceanic Technol.*, **33**, 2699–2716.

Liao, L., R. Meneghini, H. K. Nowell, and G. Liu, 2013: Scattering computations of snow aggregates from simple geometrical particle models. *IEEE J. Sel. Top. Appl. Earth Observ. Remote Sens.*, **6**, 1409–1417.

Liao, L., R. Meneghini, A. Tokay, and L. F. Bliven, 2016: Retrieval of snow properties for Ku- and Ka-band dual-frequency radar. *J. Appl. Meteor. Climatol.*, **55**,

1845–1858.

Liao, L., R. Meneghini, A. Tokay, and H. Kim, 2020: Assessment of Ku-band and Ka-band Dual-frequency radar for snow retrieval. *J. Meteor. Soc. Japan*, **98**, 1129–1146.

Liu, G., 2004: Approximation of single scattering properties of ice and snow particles for high microwave frequencies. *J. Atmos. Sci.*, **61**, 2441–2456.

Ma, Y., V. Chandrasekar, and S. K. Biswas, 2020: A Bayesian correction approach for improving Dual-frequency Precipitation Radar rainfall rate estimates. *J. Meteor. Soc. Japan*, **98**, 511–525.

Magono, C., and T. Nakamura, 1965: Aerodynamic studies of falling snowflakes. *J. Meteor. Soc. Japan*, **43**, 139–147.

Mardiana, R., T. Iguchi, and N. Takahashi, 2004: A dual-frequency rain profiling method without the use of a surface reference technique. *IEEE Trans. Geosci. Remote Sens.*, **42**, 2214–2225.

Masaki, T., T. Iguchi, K. Kanemaru, K. Furukawa, N. Yoshida, T. Kubota, and R. Oki, 2021: Calibration of the Dual-frequency Precipitation Radar (DPR) onboard the Global Precipitation Measurement (GPM) core observatory. *IEEE Trans. Geosci. Remote Sens.*, doi: 10.1109/TGRS.2020.3039978.

Meneghini, R., and H. Kim, 2017: Minimizing the standard deviation of spatially averaged surface cross-sectional data from the dual-frequency precipitation radar. *IEEE Trans. Geosci. Remote Sens.*, **55**, 1709–1716.

Meneghini, R., H. Kumagai, J. R. Wang, T. Iguchi, and T. Kozu, 1997: Microphysical retrievals over stratiform rain using measurements from an airborne dual-wavelength radar-radiometer. *IEEE Trans. Geosci. Remote Sens.*, **35**, 487–506.

Meneghini, R., H. Kim, L. Liao, J. A. Jones, and J. Kwiatkowski, 2015: An initial assessment of the surface reference technique applied to data from the dual-frequency precipitation radar (DPR) on the GPM satellite. *J. Atmos. Oceanic Technol.*, **32**, 2281–2296.

Meneghini, R., L. Liao, J. Kwiatokowki, and T. Iguchi, 2021: Path attenuation estimates for the GPM Dual-frequency Precipitation Radar (DPR). *J. Meteor. Soc. Japan*, **99**, 181−200.

Nowell, H., G. Liu, and R. Honeyager, 2013: Modeling of the microwave single-scattering properties of aggregate snowflakes. *J. Geophys. Res.: Atmos.*, **118**, 7873–7885.

Petracca, M., L. P. D'Adderio, F. Porcù, G. Vulpiani, S. Sebastianelli, and S. Puca, 2018: Validation of GPM Dual-Frequency Precipitation Radar (DPR) rainfall products over Italy. *J. Hydrometeor.*, **19**, 907–925.

Rose, C. R., and V. Chandrasekar, 2005: A systems approach to GPM dual-frequency retrieval. *IEEE Trans. Geosci.*

Remote Sens., **43**, 1816–1826.

Rose, C. R., and V. Chandrasekar, 2006a: Extension of GPM dual-frequency iterative retrieval method with DSD-profile constraint. *IEEE Trans. Geosci. Remote Sens.*, **44**, 328–335.

Rose, C. R., and V. Chandrasekar, 2006b: A GPM dual-frequency retrieval algorithm: DSD profile-optimization method. *J. Atmos. Oceanic Technol.*, **23**, 1372–1383.

Seto, S., and T. Iguchi, 2011: Applicability of the iterative backward retrieval method for the GPM Dual frequency Precipitation Radar. *IEEE Trans. Geosci. Remote Sens.*, **49**, 1827–1838.

Seto, S., and T. Iguchi, 2015: Intercomparison of attenuation correction methods for the GPM dual-frequency precipitation radar. *J. Atmos. Oceanic Technol.*, **32**, 915–926.

Seto, S., T. Iguchi, and T. Oki, 2013: The basic performance of a precipitation retrieval algorithm for the Global Precipitation Measurement mission's single/dual-frequency radar measurements. *IEEE Trans. Geosci. Remote Sens.*, **51**, 5239–5251.

Skofronick-Jackson, G., W. A. Petersen, W. Berg, C. Kidd, E. F. Stocker, D. B. Kirschbaum, R. Kakar, S. A. Braun, G. J. Huffman, T. Iguchi, P. E. Kirstetter, C. Kummerow, R. Meneghini, R. Oki, W. S. Olson, Y. N. Takayabu, K. Furukawa, and T. Wilheit, 2017: The Global Precipitation Measurement (GPM) mission for science and society. *Bull. Amer. Meteor. Soc.*, **98**, 1679–1695.

Speirs, P., M. Gabella, and A. Berne, 2017: A comparison between the GPM Dual-Frequency Precipitation Radar and ground-based radar precipitation estimates in the Swiss Alps and Plateau. *J. Hydrometeor.*, **18**, 1247–1269.

Takahashi, N., H. Hanado, K. Nakamura, K. Kanemaru, K. Nakagawa, T. Iguchi, T. Nio, T. Kubota, R. Oki, and N. Yoshida, 2016: Overview of the end-of-mission observation experiments of Precipitation Radar onboard the Tropical Rainfall Measuring Mission satellite. *IEEE Trans. Geosci. Remote Sens.*, **54**, 3450–3459.

Thurai, M., H. Kumagai, T. Kozu, and J. Awaka, 2001: Effects of incorporating a brightband model in a downward-looking radar rainfall retrieval algorithm. *J. Atmos. Oceanic Technol.*, **18**, 20–25.

Tropical Rainfall Measuring Mission, 2018: *GPM PR on TRMM reflectivity, precipitation characteristics and rate, at surface and profile L2 1.5 hours V06 (GPM_2APR)*. Goddard Earth Sciences Data and Information Services Center, doi:10.5067/GPM/PR/TRMM/2A/06.

Watters, D., A. Battaglia, K. Mroz, and F. Tridon, 2018: Validation of the GPM version-5 surface rainfall products over Great Britain and Ireland. *J. Hydrometeor.*, **19**, 1617–1636.